

# Energy & Environmental Science

Accepted Manuscript

This article can be cited before page numbers have been issued, to do this please use: M. Palmer, V. K. Singh, L. Merola, K. Natarajan Pugazhendhi, P. Barai, I. You, Y. Wang, E. Carlson, C. Wang, H. Zheng, V. Srinivasan, J. Janek, J. Sakamoto and L. Nazar, *Energy Environ. Sci.*, 2026, DOI: 10.1039/D5EE07777J.



This is an Accepted Manuscript, which has been through the Royal Society of Chemistry peer review process and has been accepted for publication.

Accepted Manuscripts are published online shortly after acceptance, before technical editing, formatting and proof reading. Using this free service, authors can make their results available to the community, in citable form, before we publish the edited article. We will replace this Accepted Manuscript with the edited and formatted Advance Article as soon as it is available.

You can find more information about Accepted Manuscripts in the [Information for Authors](#).

Please note that technical editing may introduce minor changes to the text and/or graphics, which may alter content. The journal's standard [Terms & Conditions](#) and the [Ethical guidelines](#) still apply. In no event shall the Royal Society of Chemistry be held responsible for any errors or omissions in this Accepted Manuscript or any consequences arising from the use of any information it contains.

## Broader Context

Solid-state batteries can offer higher energy densities and improved safety, but no solid electrolyte is yet simultaneously compatible with both a lithium metal anode and a high voltage uncoated cathode. Dual solid electrolyte (DSE) batteries are attractive because they can fulfill the requirements for both. However, contact of different solid electrolyte layers introduces significant challenges associated with the resulting hetero-electrolyte (H-E) interface and can yield large resistances ( $> 500 \Omega \text{ cm}^2$ ) at low stack pressures, significantly hindering battery performance. Here, we report that H-E interface resistances down to  $150 \Omega \text{ cm}^2$  can be achieved at relatively low stack pressures (i.e., 2-3 MPa) and 25 °C with a combination of soft oxyhalide catholytes and garnet separator as anolytes. Mechanical analysis and mesoscale modelling reveals that oxyhalides (hardness  $< 0.5 \text{ GPa}$ ) are significantly softer than sulfide and halide electrolytes, resulting in a larger transfer-active area at the oxyhalide|garnet H-E interface compared to a sulfide|garnet interface. Moreover, the H-E interfacial activation energy ( $E_a$ ) closely matches the grain-boundary  $E_a$  of garnet once the geometric current constriction is removed. We demonstrate that the DSE design with  $\text{LiNbOCl}_4$  and  $\text{Li}_{6.5}\text{La}_3\text{Zr}_{1.5}\text{Ta}_{0.5}\text{O}_{12}$  solid electrolytes allows for incorporation of a high voltage cathode and a Li-reservoir free anode. The DSE batteries achieve a high Coulombic efficiency ( $>99.7\%$ ) at 5 MPa and 60 °C over 120 cycles. This work demonstrates the potential for Li-reservoir free DSE batteries at low pressures.



# Conformal Hetero-Electrolyte Interface between Soft Oxyhalides and Garnet Enables Low-Pressure Lithium Reservoir-Free Solid-State Batteries

View Article Online  
DOI: 10.1039/C5EE07777J

Max Palmer<sup>Δc</sup>, Vipin K. Singh<sup>Δa</sup>, Leonardo Merola<sup>b</sup>, Karthikeyen Natarajan Pugazhendhi<sup>a</sup>, Pallab Barai<sup>d</sup>, Insang You<sup>a</sup>, Yubo Wang<sup>a</sup>, Eric Carlson<sup>c</sup>, Cathy Wang<sup>c</sup>, Hao Zheng<sup>c</sup>, Venkat Srinivasan<sup>d</sup>, Jürgen Janek<sup>b</sup>, Jeff Sakamoto<sup>c\*</sup>, Linda F. Nazar<sup>a\*</sup>

<sup>a</sup>*Department of Chemistry and the Waterloo Institute for Nanotechnology, University of Waterloo, N2L 3G1 Waterloo, Ontario, Canada*

<sup>b</sup>*Institute of Physical Chemistry and Center for Materials Research (ZfM), Justus-Liebig-University, Giessen, Heinrich-Buff-Ring 17, D-35392 Giessen, Germany*

<sup>c</sup>*Materials Department & Department of Mechanical Engineering, 1355 University of California, Santa Barbara, CA 93106-5050, United States*

<sup>d</sup>*Argonne National Laboratory, Lemont, IL, 60439, United States*

<sup>Δ</sup>*These authors contributed equally*

\*[lfnazar@uwaterloo.ca](mailto:lfnazar@uwaterloo.ca), \*[sakamoto@ucsb.edu](mailto:sakamoto@ucsb.edu)

## Abstract:

Operation of solid-state batteries with a lithium metal anode and a high voltage cathode requires solid electrolytes (SE) to be chemically stable with lithium, have a wide electrochemical window, and accommodate volume changes of the electrodes. Unfortunately, no SE exhibits satisfactory mechanical and electrochemical properties that fit these requirements to date. Dual solid electrolyte systems that use a different SE for the anolyte and catholyte present a viable solution. Here, we focus on oxyhalide SEs that demonstrate superior ionic conductivity and cathode compatibility, and where their lithium metal reactivity and poor reduction stability can be resolved using a lithium garnet (Li<sub>6.5</sub>La<sub>3</sub>Zr<sub>1.5</sub>Ta<sub>0.5</sub>O<sub>12</sub>, LLZTO) separator. Nonetheless, this imposes a new hetero-electrolyte (H-E) interface at the anolyte|catholyte contact that defines ion transport across the boundary. We report its promising properties, deconvoluted from the electrical measurements of bilayer symmetric cells, for three representative oxyhalide catholytes - LiNbOCl<sub>4</sub>, LiTaOCl<sub>4</sub>, and Li<sub>3</sub>Al<sub>3</sub>O<sub>2</sub>Cl<sub>8</sub>. Pressure-dependent measurements reveal that the relative softness of the oxyhalides (≤ 0.4 GPa) enable H-E resistances lower than 150 Ω cm<sup>2</sup> at 2-3 MPa. Mesoscale modeling reveals that the transfer-active interface of oxyhalides with LLZTO is about 2-3 fold higher compared to the argyrodite Li<sub>6</sub>PS<sub>5</sub>Cl. The low H-E resistance of the LiNbOCl<sub>4</sub>|Li<sub>6.5</sub>La<sub>3</sub>Zr<sub>1.5</sub>Ta<sub>0.5</sub>O<sub>12</sub> dual electrolyte enables cycling of a LiNi<sub>0.82</sub>Mn<sub>0.07</sub>Co<sub>0.11</sub>O<sub>2</sub>|Li full cell with a high discharge capacity (200 mAh g<sup>-1</sup>) at 60 °C and ~7 MPa.



Importantly, we demonstrate a Li reservoir-free full cell with high Coulombic efficiency (>99.5%) and capacity at 1 MPa using this approach coupled with a garnet-silver interlayer.

View Article Online

DOI: 10.1039/D5EE07777J

## Keywords

Hetero-electrolyte interface, Multilayer solid-state batteries, oxyhalide, Li metal, Garnet, reservoir-free



## Introduction

View Article Online  
DOI: 10.1039/D5EE07777J

Solid-state batteries (SSBs) have gained significant attention due to the growing demand for energy storage systems with high energy and power density.<sup>1</sup> Lithium metal - and “anode-free” or more properly termed reservoir-free designs — have been extensively studied because they offer the possibility to simplify construction, cycle ultra-pure lithium, enable high cell energy density required for SSBs.<sup>2–4</sup> Significant efforts have focused on suppressing chemo-mechanical degradation at the anode|solid electrolyte (SE) interface including dendrite growth, side reactions, and void formation.<sup>3,5,6</sup> On the cathode side of SSBs, nickel-rich  $\text{LiNi}_x\text{Mn}_y\text{Co}_z\text{O}_2$  ( $x + y + z = 1$ , NMC) offer high capacity and cell voltage, but a trade-off remains between chemical stability and mechanical compatibility at the cathode|SE interface due to highly oxidative environments and contact loss from the cathode particle volume change.<sup>7–9</sup> Different solid electrolytes are being explored for SSBs, where the most promising inorganic SE candidates can be categorized as oxyhalides/halides, oxides, and sulfides. Each has distinct chemical, electrochemical, and mechanical properties, yet no single SE meets all requirements to enable Li metal SSBs.<sup>10,11</sup>

The oxide  $\text{Li}_{6.5}\text{La}_3\text{Zr}_{1.5}\text{Ta}_{0.5}\text{O}_{12}$  (LLZTO) allows the use of a lithium metal anode (LMA).<sup>12–14</sup> While LLZTO is a brittle ceramic material with a high hardness and Young’s modulus, due to the ductility of Li it is possible to create and maintain intimate contact between the two, depending on the applied current density, temperature, and stack pressure.<sup>15–21</sup> However, there is limited compatibility of LLZTO with existing oxide cathode materials.<sup>7</sup> Degradation reactions between the LLZTO and cathode materials arise during high-temperature processes such as co-sintering that are necessary to achieve good contact, which negatively impacts performance.<sup>22,23</sup> Achieving and maintaining intimate interfacial contact in “stiff” oxide-based SSBs remains a major unresolved challenge. On the other hand, softer sulfide and halide electrolytes can achieve intimate contact with cathode materials under high fabrication pressure and moderate or room temperature, circumventing deleterious reactions. While softer than oxides, they still require high external pressure to sustain interfacial contact during operation. Generally speaking, the largest impediments to implementing sulfides and halides in SSBs are their limited electrochemical window and chemical reactivity with a LMA.<sup>24–27</sup> Typically, alternative alloy anodes, such as Li-In, are employed to avoid reactions with Li but this reduces the working voltage of the cell as well as the energy density.<sup>28,29</sup> Hardly any solid electrolyte is equally suited for reducing and oxidizing conditions at the LMA and cathode side, respectively.

Recent investigations into cell concepts utilizing dual inorganic solid electrolytes aim to combine the benefits of different SEs.<sup>29–32</sup> There are numerous reports on sulfides as the anolyte and halides as the catholyte; however, there are few definitive studies that explore the interface between



two inorganic SEs.<sup>33–35</sup> For a comprehensive review of different dual solid electrolytes explored, we refer the reader to the work by Lee et al.<sup>36</sup> While LLZTO is a superior anolyte owing to its stability with Li, there are only a few studies that implement it in dual electrolyte cells. In these cells, LLZTO acts as an anolyte in contact with the LMA and protects the catholyte from reduction, while a softer SE is used as the catholyte and forms intimate contact with the cathode active material. Dual solid electrolyte systems can fulfill the individual requirements for each electrode, but they impose a new hetero-electrolyte (H-E) interface that may have high resistances or energy barriers affecting charge transport. Factors affecting transport across such interfaces include the contact mechanics and surface topography.<sup>34</sup> These surface effects cause geometric current constriction as shown first by Fleig and Maier and then discussed for H-E interfaces by Eckhardt et al., who considered different ionic conductivity of the SEs, which governs the charge transport at the H-E interface.<sup>37,38</sup> Current constriction is significant at low stack pressures in LLZTO dual electrolyte cells and can be a major contribution to the total resistance.<sup>33–35,39</sup>

To be competitive with Li-ion batteries, achieving an H-E resistance below 20–40  $\Omega \text{ cm}^2$  remains crucial for the practical viability of dual electrolyte SSBs.<sup>40–42</sup> It remains difficult to achieve an H-E resistance near these values at relatively low stack pressures (<3–4 MPa) compared to higher pressures used for halides and sulfides. While a comprehensive guide on practical pressures for SSBs has not been elucidated, previous work by Janek and Zeier mentioned that a few MPa may be technically feasible, although 0.1 MPa is ideal to be comparable to Li-ion.<sup>10</sup> Soft solid electrolytes such as the recently explored Li metal oxyhalides that include LiNbOCl<sub>4</sub> (LNOC), LiTaOCl<sub>4</sub> (LTOC), Li<sub>3</sub>Al<sub>3</sub>O<sub>2</sub>Cl<sub>8</sub> (LAOC), as well as pliable xLiCl-GaF<sub>3</sub> composites offer several advantages towards the realization of lower and practical stack pressures.<sup>29,43–46</sup> These include a lower hardness, which facilitates densification and the ability to maintain conformal interfaces to improve cycling. Both of these aspects are simultaneously achieved, potentially at moderate pressures (~7 MPa).<sup>44,45</sup> LNOC and LTOC also exhibit a high ionic conductivity (~10 mS cm<sup>-1</sup>) that enables thicker cathodes.

Herein, we report an in-depth study of the H-E interfaces of these oxyhalide-based Li catholytes in contact with LLZTO in several cell configurations and in combination with numerous experimental techniques and computational analysis. Our work combines mechanical property analysis of the solid electrolytes via work of compression analysis and microindentation hardness measurements, interfacial analysis via X-ray photoelectron spectroscopy (XPS), and electrochemical analysis via electrochemical impedance spectroscopy (EIS) in symmetric and full cells with Li foil. We also studied Li reservoir-free cells employing a seeded silver interlayer to improve *in situ* anode formation and Coulombic efficiency. Our findings highlight the importance of achieving conformal contact under practical stack pressures and demonstrate that ion transfer across the H-E interface is governed by the mitigation of the surface passivation layer (Li<sub>2</sub>CO<sub>3</sub>/LiOH) on LLZTO. Pressure-



dependent resistance measurements support the current-constriction concept at the H-E interface.<sup>37,38</sup> Phase-field based meso-scale simulations were employed to analyze the densification of argyrodite, for comparison, and oxyhalides at different fabrication pressures, based on their experimental hardness values. This approach reveals that the transfer-active interface of LMOCs with LLZTO (i.e., the H-E contact fraction) is about 2-3 fold higher compared to the argyrodite  $\text{Li}_6\text{PS}_5\text{Cl}$ . Most importantly, we achieve low resistance – down to  $150 \Omega \text{ cm}^2$  - at lower stack pressures (i.e., 3-4 MPa) with the oxyhalides interfaced to LLZTO. A full cell utilizing single crystal  $\text{LiNi}_{0.82}\text{Mn}_{0.07}\text{Co}_{0.11}\text{O}_2$  and LMA with a LNOC catholyte and LLZTO anolyte exhibits stable cycling behavior, serving as proof-of-concept of the oxyhalide/garnet dual electrolyte approach. The full cell performance is adversely affected by the oxidation of LNOC at high voltage that is exacerbated by carbon additives. A Li reservoir-free design enabled by a seeded silver interlayer demonstrates a high Coulombic efficiency of 99.5% at 1 MPa and 60 °C. To the best of our knowledge, this study demonstrates the first Li reservoir-free solid-state cell employing an LLZTO separator without any ionic liquid or polymer at the cathode interface.

## Results and Discussion

### Properties and densification of the solid electrolytes

LLZTO and the oxyhalides were prepared in-house and characterized via X-ray diffraction (XRD; **Fig. S1**) to confirm the lack of noticeable LiCl impurity in the oxyhalides, and phase purity of LLZTO. The ionic conductivity  $\sigma_{\text{Li}^+}$  was measured by EIS in conventional symmetric cells (SS|LMOCs|SS; M = Nb, Ta, Al) and the activation energy  $E_a$  was evaluated in the temperature range from -40 °C to +40 °C. The  $\sigma_{\text{Li}^+}$  and  $E_a$  values are similar to those previously reported for LTOC and LNOC (**Fig. S2**;  $\sigma_{\text{Li}^+}$  -  $7.8 \text{ mS cm}^{-1}$ ,  $E_a$  - 0.24 eV;  $9 \text{ mS cm}^{-1}$ , 0.29 eV), LAOC (**Fig. S2**;  $0.93 \text{ mS cm}^{-1}$ , 0.46 eV), and LLZTO (**Fig. S2**;  $0.8 \text{ mS cm}^{-1}$ , 0.45 eV); see **Methods** for details.<sup>29,44</sup> To evaluate densification of the LMOCs, SE pellets were fabricated using  $\text{Li}_6\text{PS}_5\text{Cl}$  (LPSCl) as a reference. Over 300 MPa is typically used for LPSCl,<sup>39,47,48</sup> but here we used lower fabrication pressures that are more suitable for LMOCs, for comparison (i.e., 120 MPa). **Fig. 1** presents focused ion beam and scanning electron microscopy (FIB-SEM) cross-sectional images of LAOC, LNOC, and LPSCl SEs after densification at 120 MPa for 3 minutes. The LAOC SE exhibits a nearly fully dense microstructure (**Fig. 1a**) with no observable porosity. In contrast, LNOC (**Fig. 1b**) and LTOC (**Fig. S3**) have relatively dense microstructures, while LPSCl exhibits a noticeably more porous microstructure (**Fig. 1c**). The relative densities obtained for LNOC and LPSCl were 96% and 74%, based on theoretical densities of  $2.61 \text{ g cm}^{-3}$  and  $1.64 \text{ g cm}^{-3}$ , respectively.<sup>44,49</sup> The pronounced difference in relative density between LNOC and LPSCl can be attributed, at least in part, to differences in particle size distribution and the associated compaction behavior. Particle size strongly influences elastic strain



recovery upon unloading, as larger particles tend to store more elastic energy during pressing and exhibit greater spring-back once the load is removed, resulting in higher residual porosity. In contrast, smaller particles provide a higher contact area and undergo more effective plastic deformation at interparticle contacts, thereby retaining densification more efficiently after pressure release. Consequently, the comparatively lower relative density observed for LPSCl is consistent with increased elastic recovery arising from its coarser particle characteristics.<sup>50</sup> Moreover, theoretical densities of LAOC and LTOC could not be determined due to their amorphous nature. The densification behavior of the electrolyte powder was further studied by an in-die compression test in a load frame (Instron) up to 300 MPa (**Figure S4**).

The area under the force-displacement curve represents the work of compression needed to densify the powders (**Fig. 1d**).<sup>51</sup> LAOC has the lowest value of 3.1 J compared to 4.5, 4.6, and 4.7 J for LTOC, LNOC, and LPSCl, respectively. Microindentation hardness values measured for LAOC, LNOC, and LTOC are 0.18, 0.42, and 0.38 GPa, respectively (**Fig. 1e**); indentation maps and modulus measurements are given in **Fig. S5** and **Table S1**. The lower hardness of LAOC may be expected due to its viscoplasticity whereas there are no reports on LNOC and LTOC demonstrating viscoplasticity.<sup>43</sup> Due to the porosity of our LPSCl, **Fig. 1e** compares the measured LMOC microindentation hardness to the literature value of LPSCl from nanoindentation.

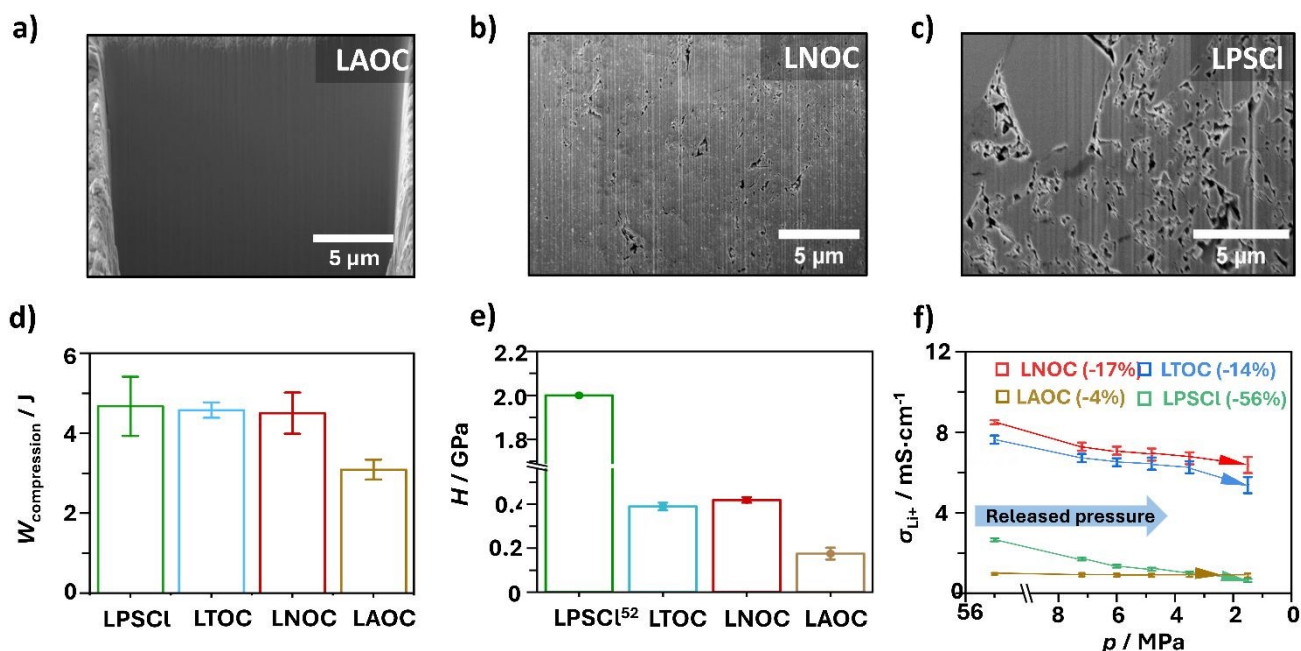


**Figure 1:** FIB-SEM cross-sectional images of (a) LAOC, (b) LNOC and (c) LPSCl, after densification at 120 MPa for 3 minutes; (d) densification behavior of SEs vs work of compression performed up to 310 MPa pressure; (e) hardness measurements of LPSCl (hot-pressed) using nano-indentation<sup>52</sup> and LMOCs ( $M = \text{Nb, Ta, Al}$ ) SEs measured via microindentation, (f) conductivity measurements during unloading from 55 MPa to lower stack pressures for LTOC, LNOC, LAOC and LPSCl. The relative change (%) in ionic conductivity upon releasing the stack pressure from 55 to 7.2 MPa is indicated in parentheses. Error bars represent the standard deviation from at least three measurements.

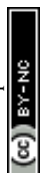


While related, it should be noted that hardness is typically strain rate-independent whereas viscoplasticity is strain rate-dependent. In the future, the viscoplastic properties of LMOCs will be studied, specifically with regard to the impact on densification and cell cycling behavior. Reported hardness values for sulfide type SEs measured via nano-indentation range from 1.4 GPa to 2 GPa,<sup>52–54</sup> depending on the synthesis protocol; thus, 2 GPa for LPSCl can be regarded as the upper limit. In contrast, the oxyhalides examined in this study exhibit up to four-fold lower hardness ( $H < 0.5$  GPa), consistent with previous reports on other chloride-based systems.<sup>32</sup> While sulfides have been considered soft SEs as they can be densified at room temperature, the lower work of compression and microindentation hardness demonstrate that LMOCs, especially LAOC, can be considerably softer.

To evaluate the influence of stack pressure on ionic conductivity, SE pellets were first densified at 120 MPa for 3 minutes, followed by EIS measurements under progressively reduced stack pressures (**Fig. 1f**). A carbon foil was employed as a compliant interfacial layer to improve the contact between the current collector (CC) and the SE, that helps to reliably measure the ionic conductivity at low stack pressures ( $< 5$  MPa).<sup>47</sup> The corresponding Nyquist plots are shown in **Fig. S6**. Among all electrolytes, LPSCl exhibits the most significant decrease in ionic conductivity (-56%) when the stack pressure is reduced from 55 to 7.2 MPa, which is consistent with a lack of densification. In contrast, LAOC shows only a minor reduction of -4% under the same unloading pressure conditions. This agrees well with the recent study by You et al. and owes to its softer and viscoplastic nature that better accommodates interfacial deformation.<sup>43</sup> Meanwhile, LNOC and LTOC display a comparatively moderate decrease of -17% and -14%, respectively. The dependence of the ionic conductivity on pressure is most likely due to a high degree of densification and therefore less elastic relaxation upon unloading. In general, it would be expected that materials with high works of compression (*i.e.*, LPSCl) will exhibit more elastic relaxation and less densification when removing the applied stress. This finding agrees well with the FIB-SEM and hardness measurements where the oxyhalides show higher densification and lower resistance to plastic deformation compared to LPSCl. The decrease in ionic conductivity with decreased pressure for the oxyhalides follows the trend in the hardness and work of compression with  $LAOC < LNOC \sim LTOC$ .

### Mesoscale modeling of densification and contact area evolution at the H-E interface

Mesoscale modelling techniques were used to understand (i) the pressure induced densification of the LPSCl and LAOC SEs, and (ii) the evolution of H-E contact fraction at the LPSCl|LLZTO and LMOC|LLZTO (M = Nb, Al) interface under different stack pressures. Creep is assumed to be the primary mechanism by which densification is achieved.<sup>55</sup> Higher pressures promote creep deformation that governs the densification in softer SEs (such as sulfides and oxyhalides). It should be noted that for the purpose of modelling the densification behavior, the yield stress



$(\sigma_y = \frac{H}{3})$  is preferred over flow stress ( $\sigma_f$ ) for LPSCI as the homologous temperature during densification at room temperature ( $T_H < 0.4$ ) and it melts congruently at 532 °C.<sup>56</sup> While  $\sigma_f$  may be more appropriate for LMOCs, it is difficult to define a melting point for LAOC due to its polymeric structure and for LNOC/LTOC due to their nanocrystalline-amorphous nature.<sup>44</sup>

View Article Online  
DOI: 10.1039/D5EE07777J

The predicted model microstructures of the SEs were densified at 120 MPa for 3 minutes at room temperature following the same experimental conditions in the section above, considering different  $\sigma_y$ . The microstructures are shown in **Fig. 2a**. For the case where yield strength is larger than the applied pressure ( $\sigma_y > P_{app}$ ), less deformation occurs resulting in a lower relative density compared to when ( $\sigma_y < P_{app}$ ).<sup>57,58</sup> Creep-induced densification at lower temperatures is particularly important for soft electrolytes such as LMOCs if sufficient pressure is applied to exceed their  $\sigma_y$ . The mesoscale model-predicted evolution of relative density with time under an applied pressure of 120 MPa, with and without the creep deformation, is shown in **Fig. 2b**. For materials with lower  $\sigma_y$  (such as LAOC - red trace), it is possible to obtain almost 100% relative density within 30 seconds due to the presence of the creep deformation induced densification (see redline in **Fig. 2b**). However, materials with higher  $\sigma_y$  (such as LPSCI) demonstrate limited creep induced densification at 120 MPa, which leads to minimal improvement in relative density, as denoted by the green trace in **Fig. 2b**. The model-predicted trend in densification is in good agreement with the experimental observations in **Figs. 1a** and **1c**.

To better understand how fabrication pressure affects the evolution of interfacial contact at the H-E interface, a separate mesoscale level model was developed for studying the LPSCI|LLZTO, LNOC|LLZTO, and LAOC|LLZTO interfaces (**Fig. 2c**). The mesoscale model begins with a flat surface for the softer catholytes (LPSCI, LNOC, and LAOC) and a rough LLZTO surface with root

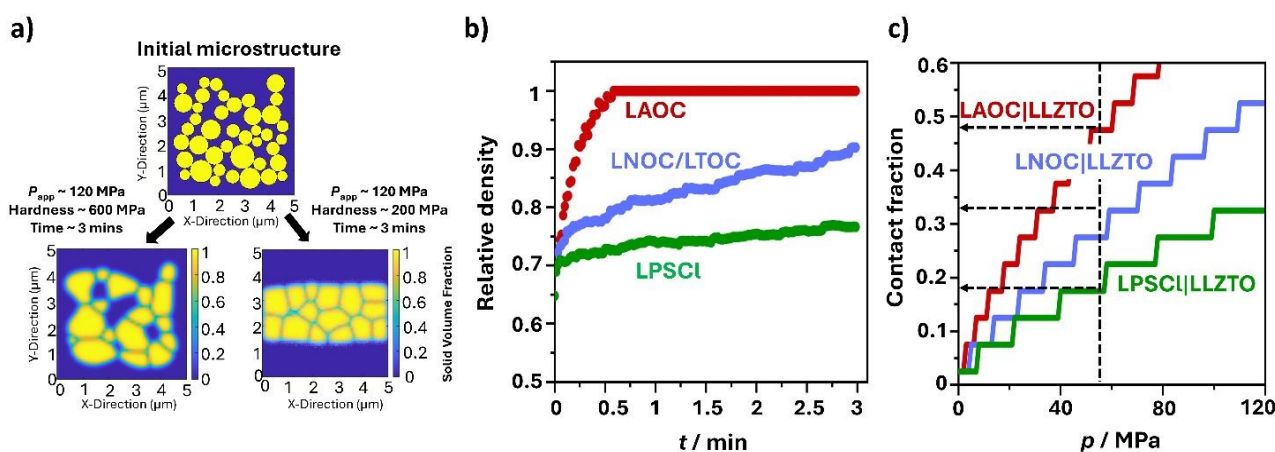


*Figure 2 : (a) Evolution of particle microstructure during the densification of LPSCI (left) and LAOC (right) SEs under 120 MPa at room temperature conditions, but with different hardness values. (b) Increase in relative density with time under an external pressure of 120 MPa for LPSCI (green trace), LNOC/LTOC (blue trace) and LAOC (red trace). (c) Increasing contact fraction of LMOCs|LLZTO H-E interface across different stack pressures.*

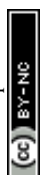


mean square roughness,  $Sq$ , of  $\sim 220$  nm was to simulate the pellet-to-pellet configuration. The evolution of interfacial contact with increasing pressure at room temperature was then analyzed. This configuration was selected to reflect the assembly conditions of the full cells fabricated in this study, as the powder-to-pellet method for densifying LMOCs on LLZTO resulted in lower Coulombic efficiency ( $\sim 98\%$ ), as discussed later. The deformed configuration of the LPSCl|LLZTO, LNOC|LLZTO, and LAOC|LLZTO interfaces at similar stack pressure (i.e., 55 MPa) used for the bilayer symmetric cells are demonstrated in **Fig. 2c**. Under a pressure of 55 MPa, LPSCl, LNOC and LAOC demonstrate 17%, 28%, and 47% H-E contact fraction respectively. In short, due to the higher  $\sigma_y$  and less creep deformation, achieving a similar contact fraction for LPSCl|LLZTO and LNOC|LLZTO requires a higher fabrication pressure. The model-predicted trends of higher transfer-active contact area enabled by softer electrolytes correlates well with the resistance evolution in the low frequency (LF, *i.e.*, H-E) interface region and its physical origin is discussed below.

### Electrical properties of bilayer symmetric cells

The kinetics at the H-E interface are not solely governed by pore-induced geometric constriction at the anolyte|catholyte interface. They are also influenced by surface passivation layers (e.g., LiOH,  $\text{Li}_2\text{CO}_3$ , etc.), which governs ionic transport between the contacted materials. Previous studies on sulfide|Al-LLZO, halide|LLZTO, and (polyethylene) oxide|LLZTO polymer systems have shown that the H-E interfacial resistance is highly sensitive to the surface chemistry of LLZTO.<sup>33–35,59</sup>

**Fig. 3** compares the resistance and activation energy ( $E_a$ ) values of LMOC|LLZTO|LMOC bilayer symmetric cells (see **methods for cell fabrication — scheme 2**) extracted from their Nyquist plots. We identify three processes in the Nyquist plots arising from bulk transport ( $>3.0$  MHz); grain boundary charge transfer (50 - 80 kHz) and the H-E interface (3 - 6 kHz) (**Fig. 3 a,b**) contributions. We note that “bulk” here refers to a superposition from resistance of  $\text{LLZTO}_{\text{Bulk}}$  and  $\text{LMOC}_{\text{total}}$ , while the grain boundary resistance only refers to  $\text{LLZTO}_{\text{GB}}$ . In the bilayer symmetric LMOC|LLZTO|LMOC ( $M = \text{Nb, Ta}$ ) cells, the first two relaxation processes align well with those of the  $\text{LLZTO}_{(\text{Bulk}+\text{GB})}$ <sup>37,60</sup> (**Fig. S7 a-c**) as seen more clearly by DRT analysis (**Fig. 3 d,e**). Notably, the low-frequency (LF) contribution associated with the H-E interfacial resistance appears only in the bilayer symmetric cells (i.e., LNOC, LTOC|LLZTO). Because the LLZTO surface was only mechanically polished, partial removal of the native passivation layer is expected. Thus, what is measured in the LF region in the LMOC|LLZTO|LMOC cells ( $M = \text{Nb, Ta}$ ), is a contribution of a more complex interface consisting of LMOC|LLZTO and a passivation layer of  $\text{Li}_2\text{CO}_3/\text{LiOH}$  on the LLZTO (which is always present). Surface roughness analyses of  $\text{Li}_6\text{PS}_5\text{Cl}|\text{Al-LLZO}$  and  $\text{Li}_7\text{P}_3\text{S}_{11}|\text{Al-LLZO}$  interfaces confirmed that geometric constriction dominates the overall resistance, with increasing roughness shifting the average time constant of the H-E interface to lower values



across all temperatures (-40 °C to +40 °C).<sup>33,35</sup> A similar trend was observed here: mechanical polishing (MP) of LLZTO pellets inside an Ar glovebox significantly affected the interfacial behavior (Fig. S8a-c). Rougher LLZTO surfaces (P400 grit,  $S_q \sim 300$  nm) exhibited lower H-E resistance than fine polished ones (P4000 grit,  $S_q \sim 30$  nm) (Fig. S8a), likely due to increased transfer-active contact area.<sup>61,62</sup> Converting the individual resistances in the time domain by performing distribution of relaxation times (DRT) analysis reveals that the interfacial contribution was prominent for fine-polished LLZTO but nearly absent for rougher surfaces (Fig. S8b). Consequently, a medium surface finish (P1000 grit,  $S_q = 120$ -150 nm) was adopted, providing a distinct H-E interface resistance and consistent deconvolution across all temperature ranges used for time constant and activation energy analysis of bilayer symmetric cells.

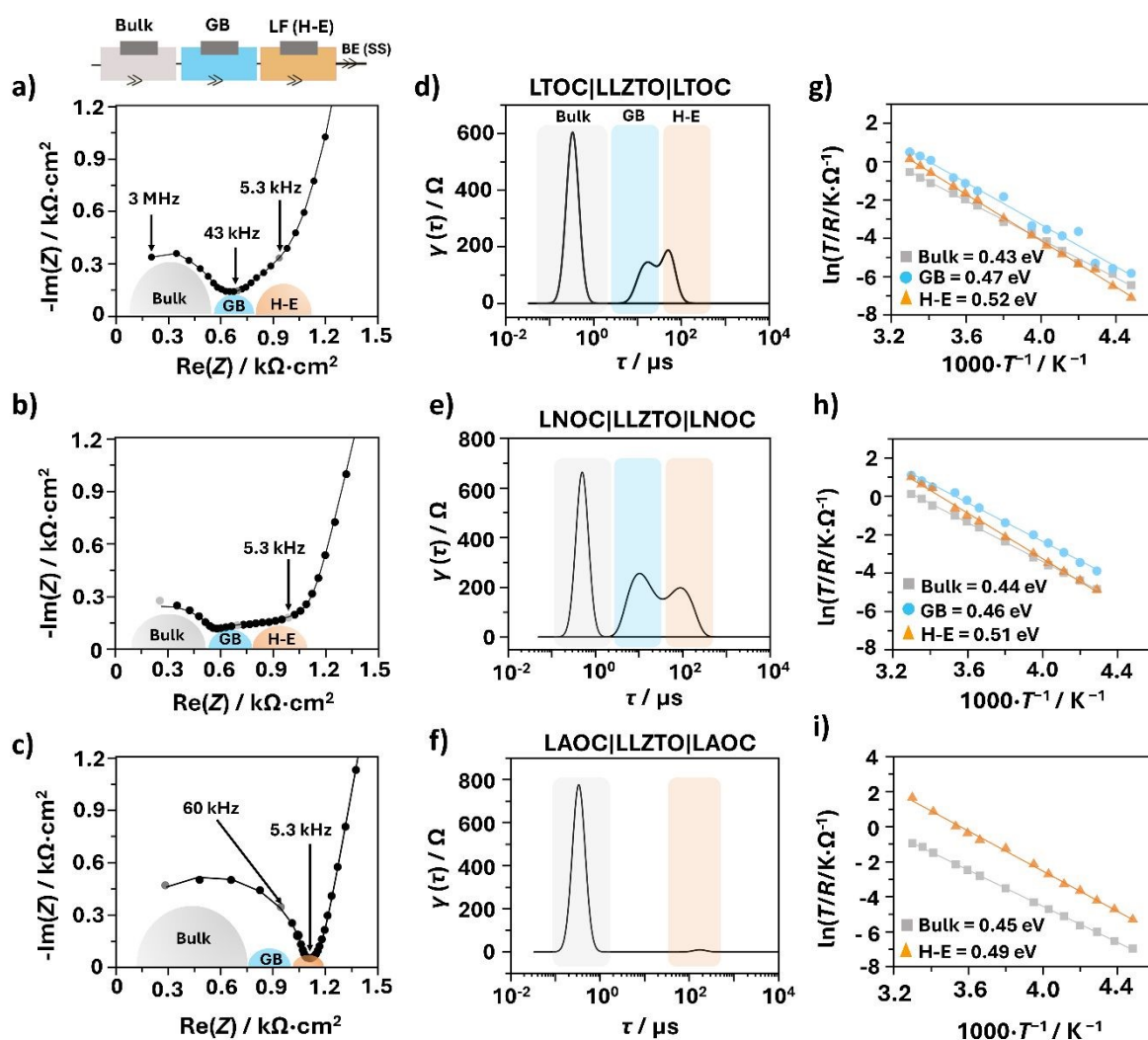


**Figure 3:** Nyquist plots collected at 55 MPa and 25 °C for the bilayer symmetric LMOC|LLZTO|LMOC cells a) LTOC; b) LNOC; c) LAOC, and (d,e,f) corresponding DRT maps. The hetero-electrolyte contribution observed at the lower frequency range (LF ~ 5 kHz) is noted by the orange shade; corresponding Arrhenius plots for g) LTOC; h) LNOC describing the activation energies for the bulk (HF), GB (MF) and H-E contributions; i) LAOC showing only the bulk (HF) and H-E (LF) contribution.



The H-E resistance and the corresponding capacitance values for the LNOC|LLZTO|LNOC and LTOC|LLZTO|LTOC bilayer symmetric cells are  $(150 \pm 24) \Omega \text{ cm}^2$ ;  $(3.6 \pm 0.1) \mu\text{F cm}^{-2}$  and  $(155 \pm 10) \Omega \text{ cm}^2$ ;  $(2 \pm 0.2) \mu\text{F cm}^{-2}$ , respectively, whereas the H-E resistance for the LAOC|LLZTO|LAOC cells are significantly smaller at  $(35 \pm 5) \Omega \text{ cm}^2$  and the capacitance is larger at  $(7 \pm 2) \mu\text{F cm}^{-2}$ . The value of resistance is doubled while the capacitance value is halved since two interfaces are measured in a symmetric cell setup, discussed above. The trend in these values agrees well with that from the FIB-SEM, work of compression, microindentation hardness measurements, and ionic conductivity relaxation from **Fig. 1**. Namely, LTOC and LNOC have near identical mechanical behavior that corresponds to similar H-E resistances and capacitances while the softer mechanical properties of LAOC correspond to a lower resistance and higher transfer-active contact area at the H-E interface as indicated by larger capacitance values than the LNOC, LTOC|LLZTO cells. Notably, in the LAOC|LLZTO|LAOC configuration (**Fig. 3c**), the grain-boundary contribution could not be resolved, likely due to similar characteristic frequencies of bulk transport in LAOC ( $\sim 70$  kHz) and the LLZTO grain boundary charge-transfer ( $\sim 60$  kHz) and the H-E interface resistance is almost negligible as confirmed from the DRT analysis (**Fig. 3f**).

Further corroboration is provided by the comparison of temperature-dependent impedance measurements to measure the respective  $E_a$  and  $\tau$  values of different processes under equilibrium conditions (*i.e.*, no current load).<sup>33,35,37</sup> For the bilayer symmetric cells, LTOC|LLZTO|LTOC and LNOC|LLZTO|LNOC configurations were investigated in this study, the  $E_a$  observed were 0.43 eV for the high-frequency (HF) region; 0.48 eV for the mid-frequency (MF) region and 0.51 eV for the low-frequency (LF), or H-E interface region (**Fig. 3g, h**). The first two energies closely match those of the HF and MF values from LLZTO<sub>(Bulk+GB)</sub> (**Fig. S2**). These activation energies are much higher than for the respective LNOC and LTOC ( $E_a \sim 0.29$  and 0.24 eV, respectively), indicating that the contribution is dominated by the LLZTO solid electrolyte with highest  $E_a$  for H-E interface, especially for LNOC, LTOC|LLZTO bilayer symmetric cells (**Fig. S9**). As noted above, the LAOC|LLZTO|LAOC cell exhibits two distinct processes corresponding to bulk transport and H-E interface, with  $E_a$  values of 0.45 eV and 0.49 eV, respectively (**Fig. 3i**). The H-E interfacial  $E_a$  closely matches the grain-boundary  $E_a$  of LLZTO, suggesting that the H-E interface behaves similarly to a grain boundary once the geometric current constriction is removed. As reported by Eckhardt et al., the largest potential drop occurs across the lower-conductivity electrolyte layer, thereby dominating the geometric current constriction.<sup>37</sup> In this case, LLZTO and LAOC possesses almost comparable ionic conductivity and the overall resistance is dominated by the bulk transport of the respective SE layer.

The average resistance values obtained from triplicate cells are summarized in **Table S2**, and the corresponding Nyquist plots recorded at  $-40^\circ\text{C}$  and 55 MPa are presented in **Fig. S10**. The



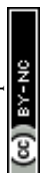
temperature dependent  $\tau$  (**Fig. S11**) of the HF and MF components are comparable to those of bulk transport in LLZTO and grain boundary charge transfer of LLZTO, respectively, whereas the H-E interface (or LF contribution) has the highest average  $\tau$  and lowest characteristic frequency, as they correlate with the relaxation time constant (**Fig. S11**). The reason for this low characteristic frequency can be related to the geometric constriction effect which may arise due to pores and passivation layers, which is common with H-E interfaces.<sup>36</sup> If full contact at the H-E interface were achieved (*i.e.*, LAOC|LLZTO cell), its characteristic frequency would instead be closer to the MF region, similar to a grain boundary (or MF) process (*i.e.*, LAOC|LLZTO cell). This demonstrates that the H-E interface would lead to a significant potential drop in dual electrolyte cells.

### Effect of passivation layers on charge transfer across the hetero-electrolyte interface

While it is well known that the surface chemistry of LLZTO impacts the charge transfer kinetics at the interface with Li metal, the hetero-electrolyte interface has been considerably less studied.<sup>33–35,63,64</sup> To quantitatively analyze the chemical components and optimize the surface chemistry of LLZTO pellets, both dry (heat treatment - HT) and wet (phosphoric acid treatment - H<sub>3</sub>PO<sub>4</sub>) methods were used to evaluate the effectiveness of the H-E interface between the LLZTO and LMOCs (**see methods for details on surface treatment of LLZTO pellets - ESI**).

The LNOC|LLZTO|LNOC bilayer symmetric cell was selected as a case study for examining the effect of removing the passivation layers on LLZTO. LNOC was chosen because it had the most discernible H-E resistance (**Fig. 3b**) that is evident in the low frequency region in the DRT analysis (**Fig. 3e**) and LNOC is a more understood material in the literature.<sup>44,65–67</sup> At the same mechanical polish finish (P1000 grit,  $S_q = 120\text{--}150$  nm), the H-E interface resistance after HT and H<sub>3</sub>PO<sub>4</sub> treatment was  $(37 \pm 25)$  and  $(41 \pm 15)$   $\Omega$  cm<sup>2</sup>, respectively (**Fig. 4a and Fig. S12**). There was a greater variability in the LMOC|LLZTO<sub>HT</sub> cells noted by the large error bars, indicating this procedure is less reproducible. This could be due to the reoccurrence of passivation layers even under Ar glovebox like conditions as reported previously by Siniscalchi et al.,<sup>68</sup> while after H<sub>3</sub>PO<sub>4</sub> treatment, the H-E interface resistance was mainly consistent and more reproducible (**Fig. 4b**). The reduced H-E resistance after the H<sub>3</sub>PO<sub>4</sub> treatment may come from increased surface roughness induced by acid etching, as reported previously.<sup>34</sup> Such surface modification likely enhances the transfer-active contact area at the LLZTO|LMOC interface, thereby facilitating ion transfer.<sup>33,35</sup> Furthermore, the  $E_a$  values after HT treatment ( $0.49 \pm 0.01$ ) eV was slightly lower than the LLZTO<sub>MP</sub> ( $0.51 \pm 0.01$ ) eV - **Fig. 4c and Fig. S12b**. In contrast, slightly higher  $E_a$  ( $0.54 \pm 0.01$ ) eV - **Fig. 4c and Fig. S12d** was observed for H<sub>3</sub>PO<sub>4</sub> treated LLZTO discs (discussed below).

The X-ray photoelectron spectroscopy (XPS) analysis of the LLZTO pellets after surface treatment is shown in **Fig. 4d(i-iv)** and **Fig. S13** and their respective H-E resistance and  $E_a$  values are



summarized in **Table S3** to clarify the surface chemistry effects. The presence of a passivating  $\text{Li}_2\text{CO}_3$  contamination layer with a thickness greater than the penetration depth of the X-rays ( $\sim 10\text{ nm}$ ) is evident in the O1s spectra corresponding to the pristine LLZTO, which obscures the underlying signal from the lattice oxygen of the garnet at  $\sim 528.9\text{ eV}$ .<sup>68,69</sup> The O1s spectrum of  $\text{LLZTO}_{\text{MP}}$  and  $\text{LLZTO}_{\text{HT}}$  reveals three major peaks, which are assigned to  $\text{Li}_2\text{CO}_3$  (531.6 eV),  $\text{LiOH}$  (530.7 eV) and the LLZTO lattice oxygen (528.9 eV).<sup>69,70</sup> Both MP and HT remove  $\text{Li}_2\text{CO}_3/\text{LiOH}$  although the HT cleans the

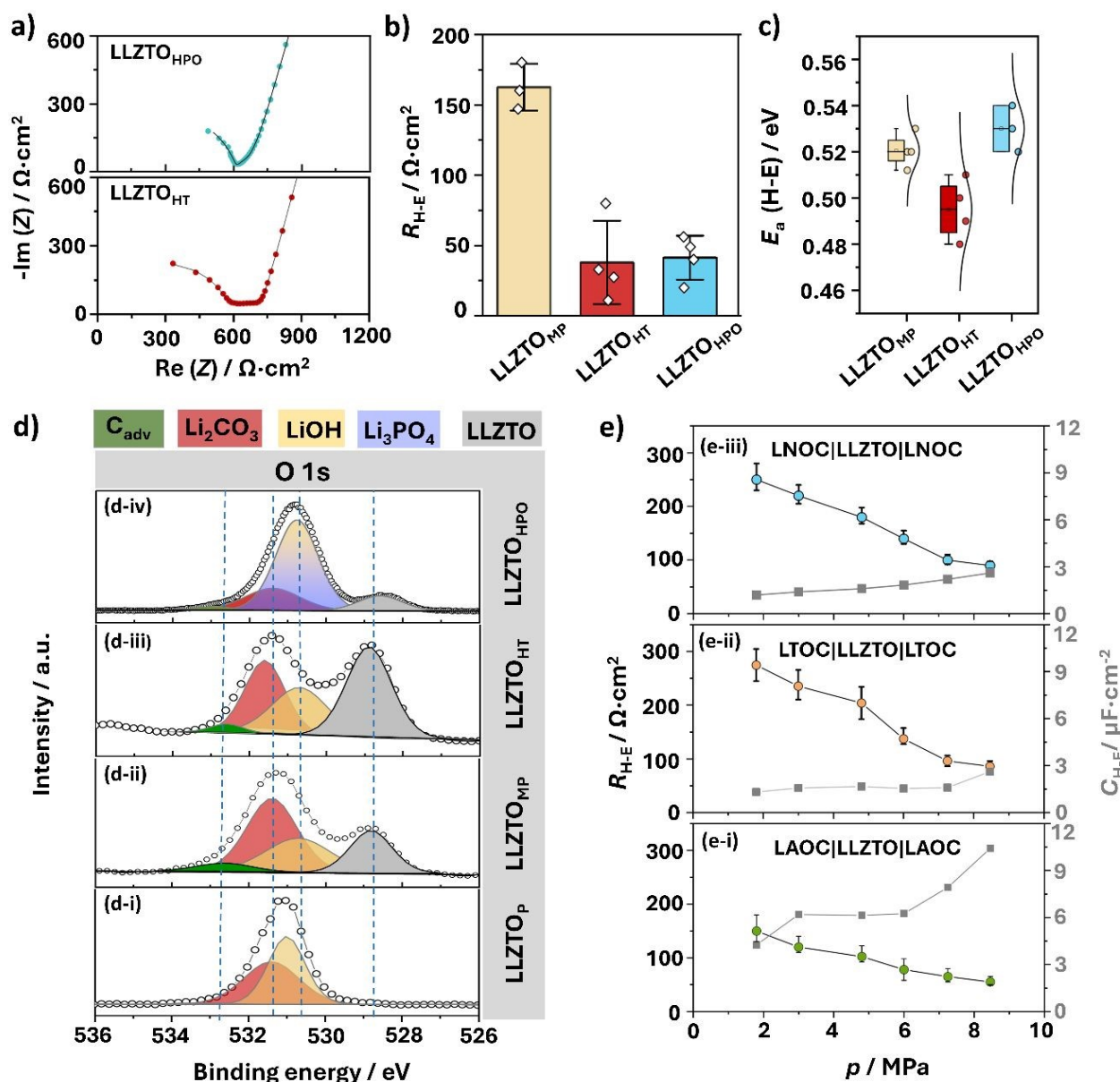


Figure 4: Comparison of the Nyquist plots of the bilayer symmetric cell (a)  $\text{SS}|\text{LNOC}|\text{LLZTO}|\text{LNOC}|\text{SS}$  at  $25\text{ }^\circ\text{C}$  and  $55\text{ MPa}$  stack pressure after phosphoric acid ( $\text{H}_3\text{PO}_4$ ), and heat treatment (HT). Comparative analysis of the (b) hetero-electrolyte resistance and (c) activation energies ( $E_a$ ) after mechanical polishing ( $\text{LLZTO}_{\text{MP}}$ ), heat treatment ( $\text{LLZTO}_{\text{HT}}$ ) and phosphoric acid ( $\text{LLZTO}_{\text{HPO}}$ ), (d) XPS analysis for O 1s spectra of ( $\text{LLZTO}_{\text{Pristine}}$ ), ( $\text{LLZTO}_{\text{MP}}$ ),  $\text{LLZTO}$  (HT),  $\text{LLZTO}$  (HPO). (e) Comparison of H-E interface for bilayer symmetric cells for  $\text{C}|\text{LNOC}|\text{LLZTO}|\text{LNOC}|\text{C}$ ;  $\text{C}|\text{LTOC}|\text{LLZTO}|\text{LTOC}|\text{C}$  and,  $\text{C}|\text{LAOC}|\text{LLZTO}|\text{LAOC}|\text{C}$ . Bar plots consist of standard deviation with at least 3 cells. The lines are a guide to the reader in e).



LLZTO more effectively as evident by the larger lattice oxygen signal. The more efficient removal of the  $\text{Li}_2\text{CO}_3/\text{LiOH}$  from the  $\text{LLZTO}_{\text{HT}}$  surface leads to the lower  $E_a$  compared to the  $\text{LLZTO}_{\text{MP}}$ .  $\text{Li}_2\text{CO}_3$  and  $\text{LiOH}$  are also present on the  $\text{H}_3\text{PO}_4$  treated LLZTO as well as a  $\text{PO}_4^{3-}$  signal (531.5 eV) that overlaps with the  $\text{Li}_2\text{CO}_3$ .<sup>71</sup> It is known that  $\text{H}_3\text{PO}_4$  treatment of LLZTO phosphorylates the metal (Li, La, Zr) ions forming a phosphate layer.<sup>69,71</sup> The lattice oxygen signal is less prominent compared to the  $\text{LLZTO}_{\text{MP}}$ , due to the metal phosphate layer consuming the bulk LLZTO signal and not due to  $\text{Li}_2\text{CO}_3/\text{LiOH}$  contamination. The metal phosphate layer also likely causes the higher  $E_a$ . Thus, HT, MP, and  $\text{H}_3\text{PO}_4$  methods are effective in removing passivation layers on the surface of LLZTO, consistent with the previous reports.<sup>69</sup>

To evaluate the impact of low stack pressure on the optimized  $\text{LLZTO}_{\text{HT}}$  surface, symmetric cells were assembled using powder-to-pellet method as previously described. The resulting effective stack pressure ranged from 1.8 to 8.2 MPa. The Nyquist plots obtained at a pressure of 1.8 MPa for bilayer symmetric LMOC|LLZTO|LMOC cells (**Fig. S14**) each clearly show the three contributions from the bulk SEs, grain boundaries of LLZTO and the H-E interface. The H-E resistance extracted from the fitting is presented in **Fig. 4e** for LAOC (**e-i**), LTOC (**e-ii**) and LNOC (**e-iii**) respectively, along with the corresponding capacitance values. As the pressure increases, a clear decrease in H-E interface resistance and increase in capacitance was observed for all three SEs, that can be attributed to geometric current constriction effects, as previously reported.<sup>37,72</sup> At the lowest stack pressure of 1.8 MPa, the H-E resistance values for LNOC and LTOC ( $250 \pm 30$ ) and ( $270 \pm 30$ )  $\Omega \text{ cm}^2$ , respectively) is almost double that of LAOC ( $150 \pm 30 \Omega \text{ cm}^2$ ) owing to the lower hardness of the latter. As mentioned, geometric current constriction resistance at the H-E interface dominates at low stack pressures and is affected by the ionic conductivity of the electrolytes (*i.e.*, higher ionic conductivity yields lower constriction resistance).<sup>37,38</sup> Even though LAOC has an order of a magnitude lower ionic conductivity than LNOC and LTOC, the H-E resistance is at least 40% lower. We believe this is a significant reduction of the interfacial resistance at low stack pressures. Thus, the mechanical properties have a larger influence on the H-E resistance than the ionic conductivity for inorganic H-E interfaces. Previous studies on the LPSC|LLZO H-E resistance reported an H-E resistance of  $9,368 \Omega \text{ cm}^2$  at 1 MPa and  $\sim 175 \Omega \text{ cm}^2$  at 30 MPa.<sup>35,39</sup> This further emphasizes the benefits of the softer LMOC electrolytes. At 6 MPa, close to the pressures that were used to run full cells (discussed below), the H-E resistance for LNOC was less than  $100 \Omega \text{ cm}^2$  and even lower for LAOC, which is promising for practical applications. The H-E interfacial capacitance at 6 MPa observed for the LMOC|LLZTO (M = Nb, Ta) cell ( $2.2, 1.6 \mu\text{F cm}^{-2}$ ) was lower compared to that of the LAOC|LLZTO cell ( $6 \mu\text{F cm}^{-2}$ ). This confirms the larger transfer-active contact area in the latter remains at low stack pressures (**Fig. 4e**).

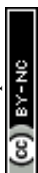


### Full cell performance with the LMOC|LLZTO dual electrolyte

After demonstrating a low and stable resistance at the LMOC|LLZTO interface, a dual electrolyte LLZTO and LNOC full cell was assembled. LNOC was chosen over LAOC and LTOC as it has the highest ionic conductivity, making it a more suitable catholyte, despite its less favorable H-E interface properties. Initially, full cells were attempted following the powder-to-pellet method as discussed above by densifying an LNOC interlayer and composite cathode against the LLZTO at 120 MPa. Full cells made with this procedure had a low Coulombic efficiency (~98%) and often shorted (**Fig. S15**). The low fabrication pressure likely leads to poor cathode density, limiting the performance. An alternative procedure is to pre-densify the LNOC and composite cathode separately at higher fabrication pressures and then integrate them together in a LLZTO|Li half-cell (pellet-to-pellet method).<sup>34</sup> This enables higher composite cathode density and uniformity, although with a consequence of higher resistance from constriction at the LMOC|LLZTO hetero-electrolyte interface.<sup>34</sup> In each full cell the LLZTO side in contact with the LNOC was treated with H<sub>3</sub>PO<sub>4</sub> for better reproducibility as shown in **Fig. 4b** despite having a high activation energy barrier across the H-E interface. In any means, full cell performance does not depend on the LLZTO surface treatment, *i.e.*, it is consistent with a heat treated or H<sub>3</sub>PO<sub>4</sub>-treated LLZTO surface as will be discussed later. Thus, full cells built with the pre-densification method are tested at a stack pressure of 7 MPa at 60 °C to lower the constriction resistance (**Fig. S16**) at the H-E (see the **Experimental for a detailed description of the cell assembly**).

Full cell investigation with a composite cathode of NMC:LNOC in a ratio of 7:3 by weight was attempted. This corresponds to a volume fraction of 57% for NMC and 43% for LNOC assuming their respective densities are 4.63 g cm<sup>-3</sup> and 2.61 g cm<sup>-3</sup>.<sup>73</sup> Only 20 mAh g<sup>-1</sup> of capacity is attained due to poor electrical wiring within the composite (**Fig. S17**) whereas the expected capacity is >180 mAh g<sup>-1</sup>. To alleviate this issue, vapor-grown carbon fibers (VGCF) were added into the composite. It is known that carbon additives exacerbate the oxidation of solid electrolytes at high voltages.<sup>74,75</sup> Thus, to elucidate the effects of carbon on the stability of LNOC at high state of charge (SOC), full cells were assembled with 2 wt% and 5 wt% VGCF while maintaining an NMC:LNOC ratio of 7:3 (schematic, **Fig. 5a**). Each experiment was repeated at least in triplicate with values reported as the average. The cells were cycled once at a C/10 rate (assuming 1C = 200 mA g<sup>-1</sup>) as an activation cycle (denoted as cycle 0) and then the current density was increased to C/5 between 2.8-4.3 V vs. Li<sup>+</sup>/Li.

The galvanostatic charge/discharge curves and performance of representative NMC|LNOC|LLZTO|Li cells are shown in **Fig. 5b,c**. The triplicate cycling data is presented in **Fig S18**. During the activation cycle, the 2 wt% and 5 wt% cells demonstrate near full utilization of the NMC with a high initial discharge capacity of (186.4 ± 8.3) and (200.1 ± 17.1) mAh g<sup>-1</sup>, respectively. The lower capacity in the 2 wt% cells is attributed to inhomogeneity in the mixing of the composite



cathode.<sup>76</sup> As each cathode was not batch processed and instead was measured and hand mixed separately, large variation from sample to sample was possible.<sup>76</sup> The 2 wt% cells exhibit less polarization during cycling compared to the 5 wt% VGCF cell (**Figure 5b**). After 25 cycles the 2 wt% cells retain  $(92.6 \pm 2.9)\%$  of the initial capacity while the 5 wt% cell only retains  $(85.0 \pm 1.0)\%$  (**Fig. 5c**) indicating more capacity deterioration as a result of LNOC degradation with higher VGCF content.

To investigate the cause of the VGCF effects on the capacity, EIS was carried out after the activation cycle and then every 5 cycles. EIS was performed at 100% SOC. Representative Nyquist plots of the 2 wt% and 5 wt% cells in the charged state are shown in **Fig. 5 d,e**, respectively. The Nyquist plots were not normalized by area as the electroactive surface area in the composite cathode is not known. The Ohmic resistance in the cells originates from the bulk conduction in LLZTO and the LNOC interlayer, although at 60 °C the time constants for the bulk transport properties are too short to be probed using a maximum of 7 MHz. The HF semicircle (0.6-0.9 MHz) is attributed to the grain boundary resistance in the LLZTO while the MF semicircle (90-200 kHz) is attributed to the

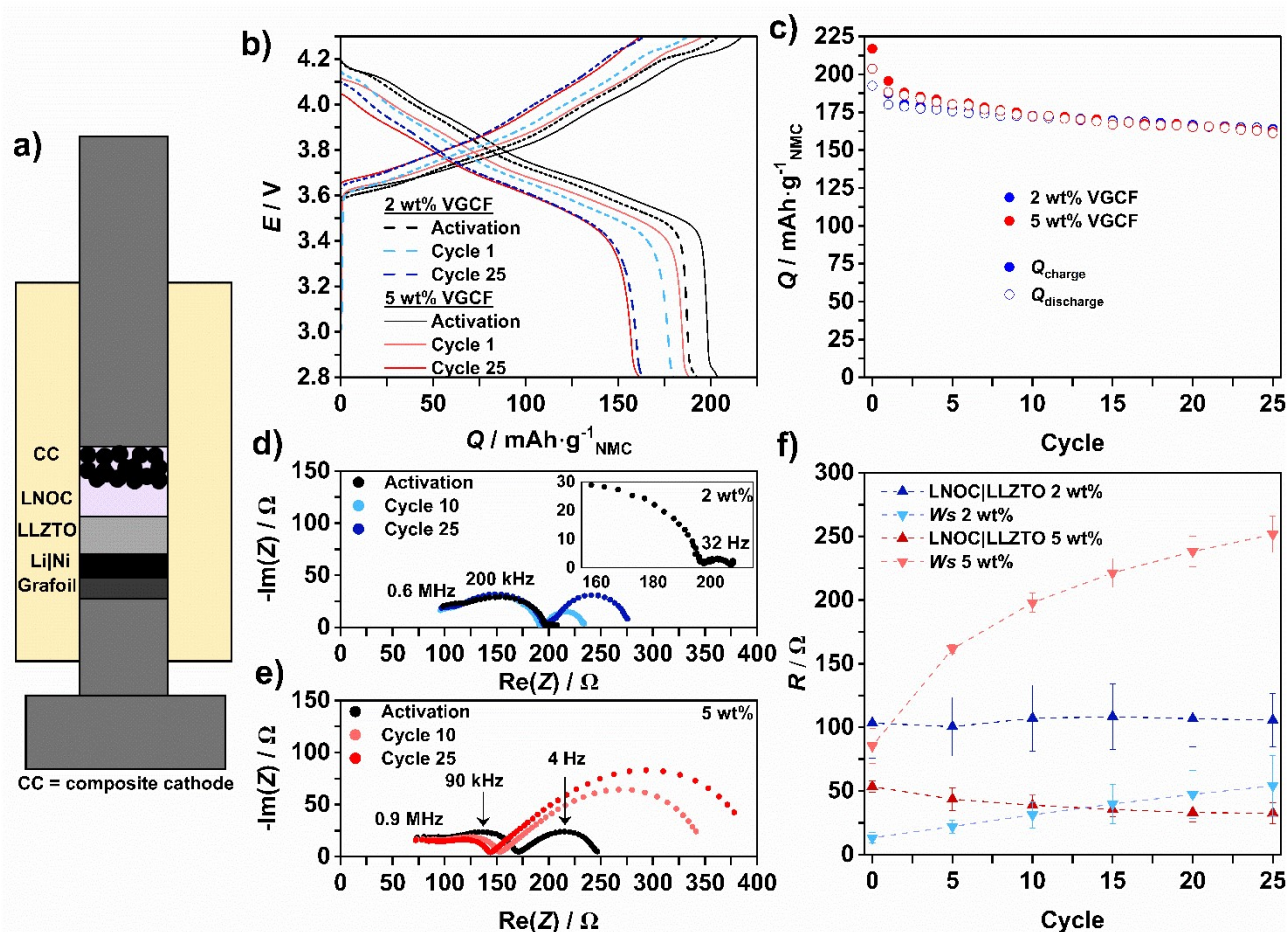


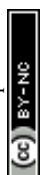
**Figure 5 :** Cell schematic of a dual electrolyte battery. **b)** Charge and discharge curves of the 2 wt % (blue) and 5 wt% (red) full cells. The voltage is vs Li<sup>+</sup>/Li. **c)** Charge/discharge capacity of the full cells. Nyquist plot in the charged state of the **d)** 2 wt% full cell and **e)** 5 wt% full cell. **f)** The LNOC|LLZTO interface and the low-frequency semicircle (*Ws*) for the full cells. The dashed lines are guidance to the eye for the reader.



LNOC|LLZTO interface. The increase in the characteristic frequencies compared to **Fig. 3** is due to the increased temperature which lowers the overall resistance and time constant. At very low frequencies ( $< 50$  Hz) where diffusion processes often dominate, we observe that a  $45^\circ$  line leads into a semicircle, which can be described by and is characteristic of a short Warburg element,  $W_s$ .  $W_s$  describes finite diffusion with a transmissive boundary. Longer diffusion lengths through an increasing interphase growth or increased tortuosity lead to a larger resistance at low frequencies. This is precisely what is observed for 5 wt% VGCF content compared to 2 wt%. As expected, a higher VGCF content increases the “electrical wiring” of the LNOC, resulting in greater interphase growth owing to oxidation of the electrolyte at high potential - thus increasing resistance which is detrimental to long-term performance. Furthermore, the  $W_s$  element naturally arises in mixed ionic-electronic conductors, such as a composite cathode.<sup>77</sup> To quantify the changes in the resistance, the charged Nyquist plots were fit with a  $R(RQ)(RQ)(W_s)$  equivalent circuit model. This model fits the data well and is shown in **Fig. S19** instead of **Fig. 5** for clarity. The resistance of the LNOC|LLZTO interface does not increase in either cell during cycling (**Fig. 5e**) and remains  $< 100 \Omega \text{ cm}^2$ , demonstrating the (electro)chemical stability of the LMOC|LLZTO interface. To further demonstrate that the elevated temperature used during cell cycling does not contribute to an increase in the H-E interfacial resistance, Nyquist plots of bilayer symmetric cells (LMOC|LLZTO, M = Nb, Al) were recorded at room temperature before and after heating the cells to  $60^\circ \text{C}$  followed by re-equilibration at room temperature (**Fig. S20a,b**). No significant changes in the impedance response were observed, indicating that thermal exposure does not induce additional interfacial resistance. Long-term stability measurements of the LNOC|LLZTO interface at  $60^\circ \text{C}$  for 300 h (**Fig. S28c**) show a stable impedance profile, suggesting that no detectable side reactions occur between the two solid electrolytes under these conditions. The LMOC|LLZTO stability agrees with previous work showing better stability at the LMOC|LLZTO interface compared to the LLZTO|sulfide interface. On the contrary, in the 5 wt% cells the process described by  $W_s$  grows from a resistance of  $(85.4 \pm 13.5) \Omega$  after the activation cycle to  $(251.6 \pm 14.2) \Omega$  after the 25th cycle. The  $W_s$  resistance is significantly smaller in the 2 wt% cells with a resistance of  $(13.2 \pm 4.1) \Omega$  after the activation cycle. While the  $W_s$  grows during cycling, the resistance remains below the initial resistance of the 5 wt% cell at  $(54.1 \pm 23) \Omega$ . Hence, 5 wt% VGCF is not necessary to electrically wire the composite cathode completely and the excess VGCF is detrimental to long-term performance through increasing resistance and a larger capacity fade. Further investigation into the origin of the  $W_s$  process and degradation of the cell is discussed later.

### Ag interlayer for Li reservoir-free batteries

Next, the effects of stack pressure on the full cell were studied with 2 wt% VGCF. A full cell was cycled at 7 MPa and then the pressure was dropped to 5 MPa, 3 MPa, and finally 1 MPa. This study



was attempted with a thin Li foil anode, although abnormal discharge curves indicated poor stripping behavior at 1 MPa. To overcome these shortcomings, the Li foil was replaced with an *in situ* formed Li anode that was improved by using a silver interlayer for two reasons. First, an interlayer of silver (Ag) or gold (Au) have been shown to improve the performance of an *in situ* formed Li anode at lower pressures.<sup>75</sup> Second, a Li reservoir-free cell allows for accurate Coulombic efficiency measurements as there is not an “infinite” Li reservoir. Here, the Ag was sputtered onto the LLZTO and then the LLZTO|Ag assembly was heat treated at 400 °C in an Ar-filled glove box. After heat treatment, de-wetting of the Ag occurs and forms discrete seeds uniformly distributed across the LLZTO surface (**Fig. 6a**). A similar de-wetting between LLZTO and Au was reported by Haslam et al.<sup>78</sup> **Fig. 6a** shows variation in the size of the Ag seeds with a majority of the seeds <1 μm in diameter and a few larger seeds with a diameter between 1 - 5.5 μm. This seeded surface morphology was hypothesized by Haslam et al. to improve contact between seeded Au, and the current collector to enable stable Li plating. Other reports have investigated the performance of flat Ag, but not *ex situ* seeded Ag.<sup>79–81</sup> Hence, the performance of the Ag seeds was characterized in a Li|LLZTO|Ag half-cell to confirm its viability as an anode interlayer. The Li|LLZTO|Ag half-cells were cycled under identical conditions to the full cell (i.e., 7 MPa, 60 °C, 2 mAh cm<sup>-2</sup> capacity) with one activation cycle at a C/10 rate. To investigate the performance at different pressures, the half-cell was cycled 5 times at 7 MPa and then the pressure was dropped to 5 MPa, 3 MPa, and 1 MPa with 5 cycles at each pressure. The activation Li plating is shown in **Fig. 6b**. Several plateaus can be seen and are attributed to Li-Ag alloying (**Fig S21**).<sup>79,80</sup>

During stripping, the overpotential remains stable up to at least ~90% depth of discharge (DoD) at each pressure (**Fig. 6c**) as determined by an inflection point in the voltage curve. Thus, the Ag seeds can enable stable stripping of 2 mAh cm<sup>-2</sup> from a thick *in situ* formed Li anode at a pressure as low as 1 MPa if the discharge is limited to 90% DoD. **Fig. 6d** shows the Coulombic efficiency (CE) at each pressure when stripped to 100% DoD. The Ag seeds yield a CE of 97.35% in the activation cycle. This increases to 99.66% by the 2<sup>nd</sup> cycle at 7 MPa. Interestingly, the CE at the slower C/10 rate of the activation cycle is lower than when stripped at C/5, which is attributed to faster kinetics in a Li-rich Li-Ag alloy.<sup>82</sup> Further discussion is in the **Supporting Information**. A relatively high average CE of 99.67% and 99.42% is maintained at 5 MPa and 3 MPa, respectively. The CE drops to ~97.61% and has a larger variance at 1 MPa indicating poorer stripping capabilities. Nevertheless, this is some of the highest reported CE for the solid-state Li-Ag interlayer system.<sup>80</sup> Furthermore, above 3 MPa the CE is near the CE of the full cell (99.55%). Therefore, the Ag interlayer should not be limiting above 3 MPa in a full cell.

SEM was utilized to investigate the morphology of the Ag in the discharged state after cycling. **Fig. S22** shows micron-sized structures covering the LLZTO surface. Ko et al. observed a similar



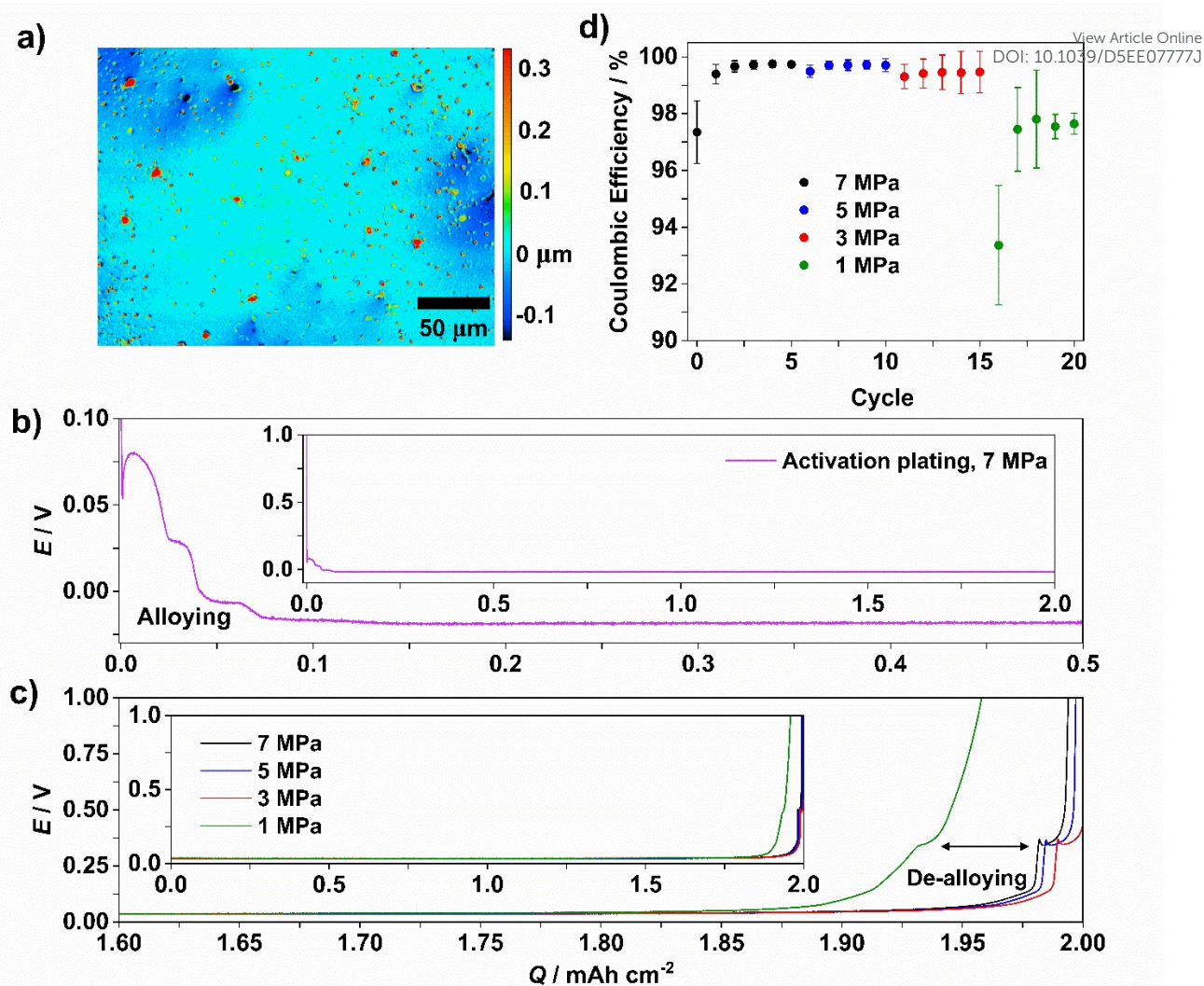


Figure 6: Laser confocal height map of the heat-treated silver (Ag) on LLZTO demonstrating the height of the Ag seeds. b) The first plating of Li to Ag during the activation cycle. The inset shows the full plating profile. c) The last stripping at each pressure at C/5. The inset shows the full stripping profile d) Coulombic efficiency of each cycle with one standard deviation. The voltage is vs.  $\text{Li}^+/\text{Li}$ .

shaped microstructure when plating Li into Ag although the structures were  $< 200$  nm in size.<sup>79</sup> Energy dispersive X-ray spectroscopy (EDX) (Fig. S22 b-d) confirms these regions are rich in Ag. As Li and Ag form a solid solution, the Ag is likely dissolved and dispersed in the plated Li.<sup>83–85</sup> During stripping the silver likely precipitates out of the shrinking *in situ* Li anode and redeposits onto the LLZTO surface.<sup>80</sup> The redeposited Ag is strongly adhered to the LLZTO surface. Upon removing the current collector, the Ag remained adhered to the LLZTO. Similarly, the redeposited Ag could only be removed from the LLZTO by scratching with a razor blade, further demonstrating the strong adhesion. This adhesion and redeposition onto the LLZTO surface in a similar distribution and size.

### Li reservoir-free full cell

After confirming the viability of Ag seeds as an anode interlayer, the Ag was incorporated into Li reservoir-free full cells. The Li reservoir-free cells were activated at C/10 and 7 MPa and then cycled 5 times at 7 MPa followed by lowering the stack pressure to 5 MPa, 3 MPa, and then 1 MPa. A



representative full cell is shown in Fig. 7a. A Li reservoir-free full cell with a heat-treated LLZTO

View Article Online

DOI: 10.1039/D5EE07777J

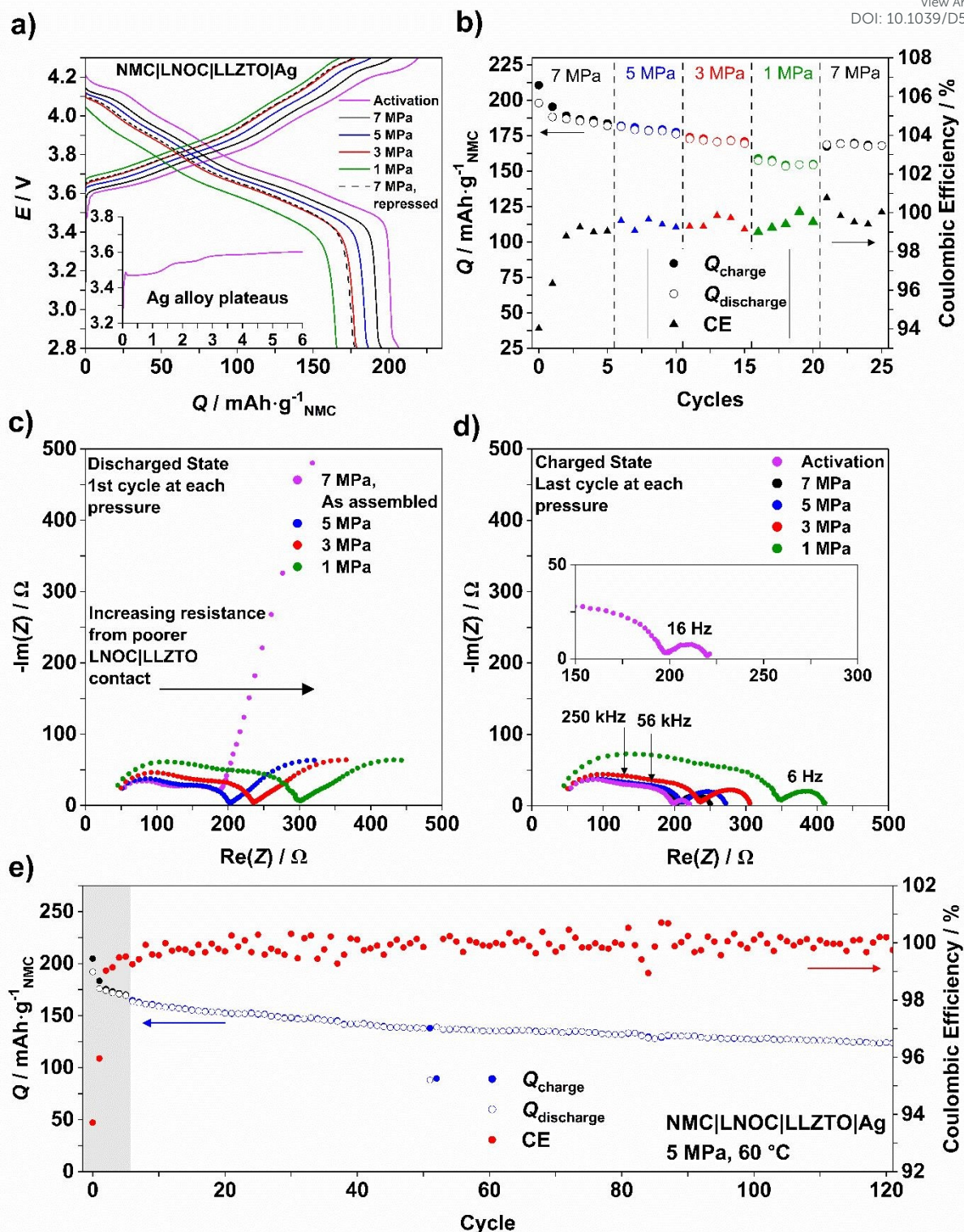


Figure 7: Cycling data for an NMC|LNOC|LLZTO|Ag Li reservoir-free full cell with an areal loading ( $\sim 2 \text{ mAh cm}^{-2}$ ). a) The first charge/discharge curve at each pressure. The inset shows a magnification of the activation cycle highlighting the Li-Ag alloying plateaus. b) Capacity and Coulombic efficiency at different pressures. c) Nyquist plots in the discharged state prior to cycling at each pressure. d) Nyquist plots of the last cycle at each pressure in the charged state. The inset is a magnification to show the low frequency part of the activation plot. e) Extended cycling of an NMC|LNOC|LLZTO|Ag Li reservoir-free full cell ( $\sim 2 \text{ mAh cm}^{-2}$ ). The activation and first 5 cycles were performed at 7 MPa (gray box). The drop in capacity near the 51<sup>st</sup> cycle was due to a connection issue.



surface (**Fig. S18c**) shows identical performance to the  $\text{H}_3\text{PO}_4$  treated LLZTO. The alloying plateaus of Ag are noticeable within the first 6 mAh  $\text{g}^{-1}$  of the activation charge shown in the inset in **Fig. 7a**. The Li reservoir-free cells have a high activation discharge capacity of  $(203.2 \pm 4.5)$  mAh  $\text{g}^{-1}$ . This high discharge capacity is comparable to the Li reservoir-free silver-carbon layer reported by Lee et al.<sup>86</sup> The activation cycle CE is  $(94.08 \pm 0.06)\%$  and at the end of discharge no de-alloying plateaus are observed. This implies the polarization of the Ag is minimal and remains in the flat Ohmic region described in the previous section. Thus, the polarization in the cell is dominated by the NMC and demonstrates that the Ag is not limiting. After the first two cycles, the cells have a high average CE of 99.57% across all pressures. This agrees well with the CE above 3 MPa in Li|LLZTO|Ag half-cell characterization. Interestingly, at 1 MPa the full cell delivers a higher CE than in the half-cell. This may be due to more Li lost in the full cell compared to the half-cell yielding a more Li-rich Li-Ag interlayer. The cells maintain high capacity and a consistent fade down to 3 MPa (**Fig. 7b**). By decreasing the pressure to 1 MPa the cell began to fade faster. Further work is to be carried out investigating the full cell performance at lower current densities to separate the anode and cathode contributions to the capacity fade.

Representative Nyquist plots of a full cell at each pressure are shown in **Fig. 7c**. It can be seen from the Nyquist plots that the total cell resistance increases upon lowering the pressure by the increase to higher resistances. Previous work has shown that constriction resistance at the LLZTO|halide and LLZTO|sulfide interface increases when lowering the stack pressure.<sup>33–35</sup> The individual resistance contributions from LLZTO and the LNOC|LLZTO interface are shown in **Fig. S23**. There is negligible change in the LLZTO and LNOC|LLZTO resistance by decreasing the pressure from 7 to 5 MPa, a small change at 3 MPa, and a significant change at 1 MPa. The increase in the LLZTO resistance is due to the loss of contact at the LNOC|LLZTO interface and current collector|cathode interface.<sup>34,87</sup> With an increase in cell resistance, a larger overpotential when cycling will exist that leads to premature cell polarization. Thus, the capacity at lower stack pressures, especially at 1 MPa, is limited by the LNOC|LLZTO interface. Nevertheless, at 1 MPa the cells still deliver a capacity of  $(157.6 \pm 8.0)$  mAh  $\text{g}^{-1}$  on the 16<sup>th</sup> cycle. This demonstrates that while the LNOC|LLZTO interface remains stable during cycling, the initial resistance from constriction currently remains a challenge at low pressures (*i.e.*, 1 MPa) for LNOC|LLZTO dual electrolyte SSBs as the original Ag seeds allows for the high CE and stable cycling.

**Fig. 7d** shows the Nyquist plots of the charged cells during the last cycle at each pressure. The LF resistance continues to grow during cycling as expected, although there appears to be no pressure dependence (**Fig. S24**). From 7 to 3 MPa the LF resistance growth behavior is similar to the Li anode cell at 7 MPa (**Fig. S24**). However, the LF resistance drops unexpectedly at 1 MPa and then rebounds higher at 7 MPa. If lower pressures cause worst contact loss, it would be expected that the

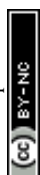


resistance at 1 MPa would increase and not decrease. A decrease in cell resistance at lower pressures frequently indicates a soft short or a dendrite. No voltage fluctuations in the charge/discharge curves indicate a soft short. To confirm there are no dendrites the LLZTO was removed after cycling (**Fig. S25**) shows both sides of the LLZTO confirming no dendrites are the cause for the resistance decrease at 1 MPa. Furthermore, the LNOC interlayer remains white/tan. If there was Li penetration through the LLZTO, the LNOC would have turned black. In any matter, a LNOC|LLZTO dual electrolyte enables high Coulombic efficiency of an *in situ* Li anode at 1 MPa. **Fig. 7e** confirms Li reservoir-free cells can operate at 5 MPa for longer cycling as well. Due to minimal resistance change from 7 to 5 MPa, longer term cycling was carried out at 5 MPa on one cell (**Fig. 7e**). The cell maintains a high Coulombic efficiency (~99.8% on average) with 70% capacity retention after 120 cycles.

### Degradation Characterization

Next, the cause of the resistance growth and capacity fading was investigated. A shortcoming of two electrode full cells is the convoluted LF behavior of both the anode and cathode. Due to the difficulty of implementing a reference electrode into the cell, a Li|LLZTO|Li symmetric cell (**Fig. S26**) and an NMC|LNOC|NMC symmetric cell (**Fig. S27**) were assembled and characterized to deconvolute the LF processes in the Nyquist plot. To create an NMC|LNOC|NMC symmetric cell with a composite cathode at 100% SOC, a full cell was first assembled and charged to 4.3 V (**Fig. S26a**). The charged composite cathode was then incorporated into the NMC|LNOC|NMC symmetric cell, densified (**Fig. S27b**) and heated to 80 °C (**Fig. S27c**). The results are shown in the **Supplementary Information**, which confirm the LF resistance is from the cathode.

To further characterize the parasitic reactions at high states of charge a full cell with 5 wt% VGCF was assembled and charged to 4.3 V. Once at 4.3 V the cell was rested at open circuit conditions and EIS was conducted every 2 hours. Prior to charging, the cell was rested for 18 hours to determine if there were any parasitic reactions in the discharged state as has recently been reported for  $\text{Li}_3\text{InCl}_6$  and NMC.<sup>88</sup> The unchanged Nyquist plot in **Fig. S20d** confirms that at low SOC there are no reactions within the composite cathode. While resting at OCV after being charged to 4.3 V, the semicircle continues to grow over 18 hours as shown in the Nyquist plot in **Fig. 8a**. This behavior was described for  $\text{Li}_{10}\text{GeP}_2\text{S}_{12}$  (LGPS) and attributed to a diffusion-controlled cathode-electrolyte interphase (CEI).<sup>9</sup> Similar diffusion-controlled interphase growth was shown for the interface between various sulfides and Li.<sup>26,75</sup> The change in resistance over time is fit to a Wagner-type CEI growth model with the resistance dependent on  $t^{1/2}$ .<sup>9,26</sup> **Fig. 8b** shows a linear trend and fits the model well. From the model, the slope of the linear trend line,  $k'$ , describes the CEI growth rate. Here,  $k' = (22.7 \pm 2.5) \Omega \text{ hr}^{-1/2}$  at 60 °C. The higher temperature influences the rate constant by lowering the resistance and so Zuo et al. introduced  $k''$ , the rate constant normalized to the initial resistance.<sup>9</sup> Here,



$k'' = 0.536 \text{ hr}^{-1/2}$  close to  $k''$  of  $\sim 0.5 \text{ hr}^{-1/2}$  for the NMC|LGPS CEI at  $40^\circ\text{C}$ . Thus, at high SOC, higher VGCF content exacerbates a parasitic reaction at the NMC|LNOC interface which leads to faster cell degradation.

In the work on the NMC|LGPS interface, it was also shown that the CEI capacitance decreases parabolically over time. **Fig. 8c** shows the change in  $W_s$  capacitance during the OCV rest showing a parabolic curve, which agrees with the model. Interestingly, from analyzing the  $W_s$  capacitance (**Fig. S28**) in the cycled full cell from **Fig. 5**, the capacitance does not decrease parabolically but instead increases parabolically. As the capacitance does not follow the expected trend, it can be concluded that there are at least two separate causes underlying the response of the LF capacitance. Currently, the explanation for the increase in capacitance is not well understood. To elucidate the (electro)chemical degradation of LNOC, XPS was performed on the composite cathodes cycled and

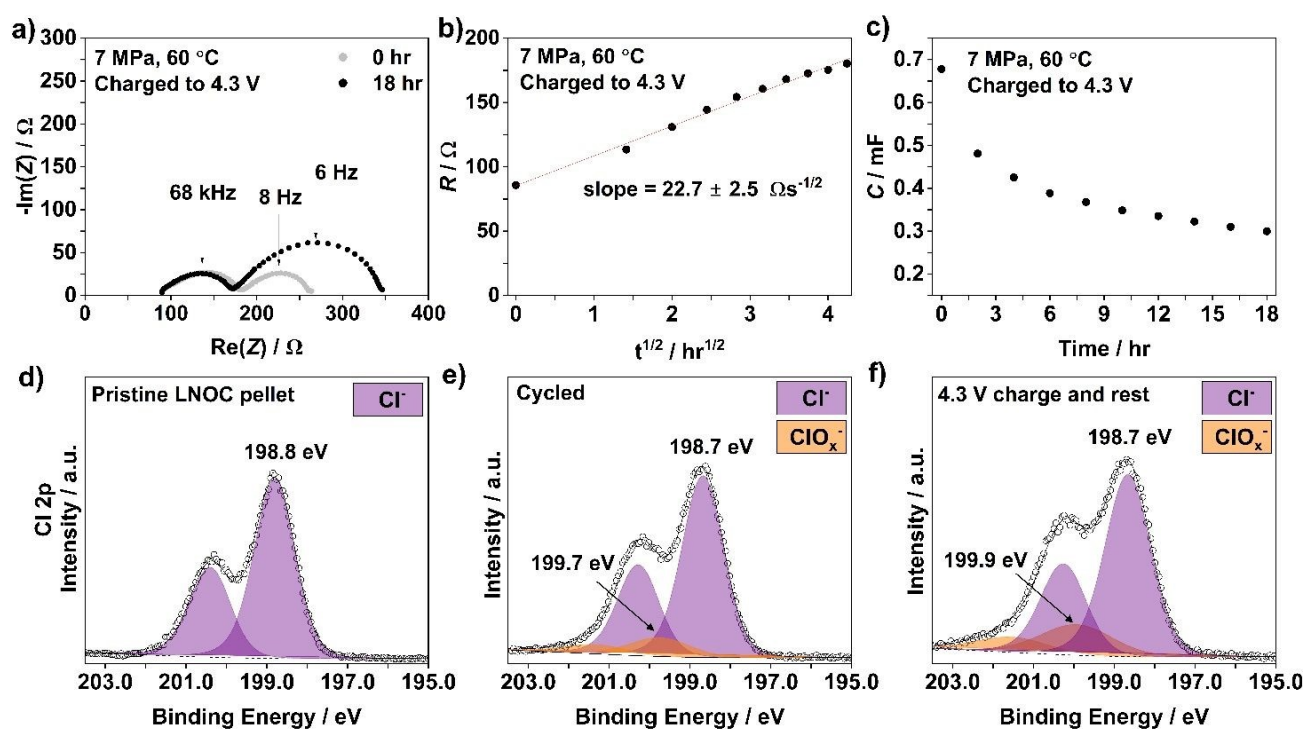


**Figure 8:** a) Time evolution Nyquist plots of a full cell charged to 4.3 V and rested at OCV. b) The Warburg resistance changes over time fit to a parabolic growth function. c) Capacitance of the Warburg element over time from a). Cl 2p spectra of c) pristine LNOC, d) composite cathode cycled 25 times, and e) composite cathode charged to 4.3 V and rested.

charged to 4.3 V and rested. In the Cl 2p spectrum, pristine LNOC shows one peak at 198.8 eV and is assigned to the Cl  $2p_{3/2}$  from bulk LNOC (**Fig. 8d**). This is close to the value reported by Jeon et al. of 198.6 eV.<sup>65</sup> After 25 cycles a broad second peak appears at 199.7 eV that is attributed to the oxidation of chloride and the formation of  $\text{ClO}_x^-$  species.<sup>65,89,90</sup> The same peak is observed in the cell charged to 4.3 V and rested, albeit more pronounced (**Fig. 8b, c**). Thus, resting at high voltages promotes more oxidation than cycling as the cell is at high states of charge for a longer time which



enhances the growth of CEI. This is contrary to a larger LF resistance from cycling. This may be due to mechanical contact loss from NMC|LNOC delamination.<sup>8,91</sup> To investigate the degree of delamination in the composite cathode, FIB-SEM was conducted. **Fig. S29** shows a comparison of a pristine cathode to cathodes cycled 25 times in the discharged and charged state. The pristine cathode shows residual porosity and incomplete densification. In the cycled cathodes, delamination between LNOC and NMC can be seen, however, as the pristine cathode has porosity and incomplete densification cathode it is difficult to quantify the degree of delamination from cycling. Nevertheless, the delamination increases the LF resistance from increased diffusion lengths (i.e., increasing tortuosity).<sup>77,92,93</sup>

## Conclusions

Our in-depth study of the LMOC|LLZTO hetero-electrolyte interface for dual electrolyte SSBs (via EIS, electron microscopy, microindentation hardness, and work of compression measurements) quantifies the soft mechanical properties of the LMOCs that enable lower fabrication and operation pressure compared to state-of-the-art sulfide electrolytes such as argyrodite. The soft nature of LMOCs also enables a conformal LMOC|LLZTO interface at room temperature and at low stack pressures leading to a H-E resistance  $< 250 \Omega \text{ cm}^2$  for LNOC and LTOC, and  $< 150 \Omega \text{ cm}^2$  for LAOC at 1.8 MPa. This work demonstrates the more critical role of the mechanical properties over the ionic conductivity in forming a low H-E resistance. While there is a low LMOC|LLZTO H-E resistance formed by densifying the LMOCs against the LLZTO, challenges remain for incorporating this design into a full cell. By pre-densifying the LNOC and cathode - and through a combination of the soft properties of LNOC, the Li stability with LLZTO, and a seeded silver interlayer - a Li reservoir-free LNOC|LLZTO full cell maintains high capacity ( $\sim 170 \text{ mAh g}^{-1}$ ) and Coulombic efficiency ( $> 99.5\%$ ) down to 1 MPa at 60 °C. A Li-reservoir free cell demonstrated exceptional Coulombic efficiency ( $\sim 99.8\%$ ) for 120 cycles at 5 MPa, maintaining 70% of the initial capacity. The capacity fade is related to oxidation of LNOC and mechanical contact loss at the NMC|LNOC interface that presents as a short Warburg at low frequencies in the Nyquist plots. This degradation could be mitigated by optimizing the LNOC and conductive additive ratios in the cathode composite to improve the effective ionic and electronic transport, thereby reducing tortuosity and polarization during cycling. Nevertheless, the LNOC|LLZTO H-E remains stable during cycling further emphasizing the LMOC|LLZTO stability. More work is needed to address incorporating the low H-E resistance into a full cell at room temperature, but this work demonstrates the potential for Li reservoir-free SSBs at low pressures through an LMOC|LLZTO dual electrolyte system.



## Author contributions:

View Article Online  
DOI: 10.1039/D5EE07777J

**Max Palmer:** conceptualization, investigation, methodology, data curation, writing - original draft, review, and editing; **Vipin K. Singh:** conceptualization, investigation, methodology, data curation, writing - original draft, review, and editing; **Leonardo Merola:** XPS formal analysis, writing - review and editing; **Karthikeyen Natarajan Pugazhendhi:** assisted with the bilayer symmetric cell fabrication; **Pallab Barai:** mesoscale modelling investigation, validation; **Insang You:** synthesis of LAOC SE; **Yubo Wang:** assisted with the synthesis of LNO and LTO; **Eric Carlson:** full cell validation; **Hao Zheng:** full cell validation; **Cathy Wang:** cathode FIB-SEM; **Venkat Srinivasan:** review and validation; **Jürgen Janek:** writing - review and editing, funding acquisition, conceptualization, supervision; **Jeff Sakamoto:** writing - review and editing, funding acquisition, conceptualization, supervision; **Linda F. Nazar:** writing - review and editing, funding acquisition, conceptualization, supervision.

## Data availability:

The data supporting this article have been included as part of the ESI. †

## Conflict of interest:

The authors declare no competing financial interests.

## Acknowledgements

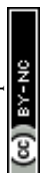
The authors would like to acknowledge Travis Casagrande (Canadian Center for Electron Microscopy) for assisting in the FIB-SEM analysis; and Hiruy Haile, Ennis Solorzano (University of Waterloo) for designing the electrochemical cell setup with force sensors. We thank Seneca Stevens (UCSB) for assistance with mechanical properties analysis and Shu-wen Zhou (UW) for help with full-cell fabrication, Dr. Baltej Singh and Dr. Insang You for the many useful discussions, and Travis Casagrande (Canadian Center for Electron Microscopy) for help with the FIB-SEM.

This work was conducted as part of the US-German project collaboration on "Interfaces and Interphases in Rechargeable Li-metal based Batteries" supported by the US Department of Energy (DOE) and the German Federal Ministry of Education and Research (BMBF). L.F.N, V.K.S, K.P, are grateful to the Ontario Research Fund (ORF-RE) for major financial support and NSERC for platform support through the Discovery Grant and Canada Research Chair program. M.P. and J.S. acknowledge financial support from the Mechano-chemical Understanding of Solid Ion Conductors, an Energy Frontier Research Center funded by the U.S. Department of Energy, Office of Science, Office of Basic Energy Science under grant no. DE-SC0023438. L.M. and J.J. acknowledge financial support from the German Federal Ministry of Education and Research (BMBF) under the project "CatSE 2" (grant identifier 03XP0510E). P.B. and V.S. acknowledge the support provided by the Assistant Secretary for Critical Minerals and Energy Innovation (CMEI), Office of Vehicle Technologies of the U.S. Department of Energy under Contract No. DE-AC02-06CH11357 through the Advanced Battery Materials Research (BMR) program.



## References

1. P. Albertus, S. Babinec, S. Litzelman and A. Newman, *Nat Energy*, 2017, **3**, 16–21.
2. M. J. Wang, E. Carmona, A. Gupta, P. Albertus and J. Sakamoto, *Nature Communications*, 2020, **11**, 5201.
3. S. E. Sandoval, C. G. Haslam, B. S. Vishnugopi, D. W. Liao, J. S. Yoon, S. H. Park, Y. Wang, D. Mitlin, K. B. Hatzell, D. J. Siegel, P. P. Mukherjee, N. P. Dasgupta, J. Sakamoto and M. T. McDowell, *Nat. Mater.*, 2025, **24**, 673–681.
4. K. B. Hatzell, *ACS Energy Lett.*, 2023, **8**, 4775–4776.
5. K. Lee, E. Kazyak, M. J. Wang, N. P. Dasgupta and J. Sakamoto, *Joule*, 2022, **6**, 2547–2565.
6. X. Zhang, Q. J. Wang, K. L. Harrison, K. Jungjohann, B. L. Boyce, S. A. Roberts, P. M. Attia and S. J. Harris, *J. Electrochem. Soc.*, 2019, **166**, A3639–A3652.
7. Y. Ren, T. Danner, A. Moy, M. Finsterbusch, T. Hamann, J. Dippell, T. Fuchs, M. Müller, R. Hoft, A. Weber, L. A. Curtiss, P. Zapol, M. Klenk, A. Ngo, P. Barai, B. Wood, R. Shi, L. Wan, T. W. Heo, M. Engels, J. Nanda, F. H. Richter, A. Latz, V. Srinivasan, J. Janek, J. Sakamoto, E. D. Wachsman and D. Fattakhova-Rohlfing, *Advanced Energy Materials*, 2023, **13**, 2201939.
8. R. Koerver, I. Aygün, T. Leichtweiß, C. Dietrich, W. Zhang, J. O. Binder, P. Hartmann, W. G. Zeier and J. Janek, *Chem. Mater.*, 2017, **29**, 5574–5582.
9. T.-T. Zuo, R. Rueß, R. Pan, F. Walther, M. Rohnke, S. Hori, R. Kanno, D. Schröder and J. Janek, *Nat Commun*, 2021, **12**, 6669.
10. J. Janek and W. G. Zeier, *Nat Energy*, 2023, **8**, 230–240.
11. K. Kerman, A. Luntz, V. Viswanathan, Y.-M. Chiang and Z. Chen, *J. Electrochem. Soc.*, 2017, **164**, A1731–A1744.
12. A. Sharafi, E. Kazyak, A. L. Davis, S. Yu, T. Thompson, D. J. Siegel, N. P. Dasgupta and J. Sakamoto, *Chemistry of Materials*, 2017, **29**, 7961–7968.
13. J. G. Connell, T. Fuchs, H. Hartmann, T. Krauskopf, Y. Zhu, J. Sann, R. Garcia-Mendez, J. Sakamoto, S. Tepavcevic and J. Janek, *Chemistry of Materials*, 2020, **32**, 10207–10215.
14. C. Ma, Y. Cheng, K. Yin, J. Luo, A. Sharafi, J. Sakamoto, J. Li, K. L. More, N. J. Dudney and M. Chi, *Nano letters*, 2016, **16**, 7030–7036.
15. Y. Kim, H. Jo, J. L. Allen, H. Choe, J. Wolfenstine and J. Sakamoto, *Journal of the American Ceramic Society*, 2016, **99**, 1367–1374.
16. S. Yu, R. D. Schmidt, R. Garcia-Mendez, E. Herbert, N. J. Dudney, J. B. Wolfenstine, J. Sakamoto and D. J. Siegel, *Chemistry of Materials*, 2016, **28**, 197–206.
17. G. Yan, J. F. Nonemacher, H. Zheng, M. Finsterbusch, J. Malzbender and M. Krüger, *J Mater Sci*, 2019, **54**, 5671–5681.
18. G. Han, B. Kinzer, R. Garcia-Mendez, H. Choe, J. Wolfenstine and J. Sakamoto, *Journal of the European Ceramic Society*, 2020, **40**, 1999–2006.
19. M. J. Wang, R. Choudhury and J. Sakamoto, *Joule*, 2019, **3**, 2165–2178.
20. W. Zaman, L. Zhao, T. Martin, X. Zhang, Z. Wang, Q. J. Wang, S. Harris and K. B. Hatzell, *ACS Appl. Mater. Interfaces*, 2023, **15**, 37401–37409.
21. J. E. Ni, E. D. Case, J. S. Sakamoto, E. Rangasamy and J. B. Wolfenstine, *Journal of Materials Science*, 2012, **47**, 7978–7985.
22. T. Demuth, T. Fuchs, F. Walther, A. Pokle, S. Ahmed, M. Malaki, A. Beyer, J. Janek and K. Volz, *Matter*, 2023, **6**, 2324–2339.
23. L. Miara, A. Windmüller, C.-L. Tsai, W. D. Richards, Q. Ma, S. Uhlenbruck, O. Guillon and G. Ceder, *ACS Appl. Mater. Interfaces*, 2016, **8**, 26842–26850.
24. L. M. Riegger, R. Schlem, J. Sann, W. G. Zeier and J. Janek, *Angewandte Chemie*, 2021, **133**, 6792–6797.
25. L. M. Riegger, S.-K. Otto, M. Sadowski, S. Jovanovic, O. Kötz, S. Harm, L. G. Balzat, S. Merz, S. Burkhardt, F. H. Richter, J. Sann, R.-A. Eichel, B. V. Lotsch, J. Granwehr, K. Albe and J. Janek, *Chem. Mater.*, 2022, **34**, 3659–3669.



26. S. Wenzel, S. J. Sedlmaier, C. Dietrich, W. G. Zeier and J. Janek, *Solid State Ionics*, 2018, **318**, 102–112. View Article Online  
DOI: 10.1039/D5EE07777J
27. G. F. Dewald, S. Ohno, M. A. Kraft, R. Koerver, P. Till, N. M. Vargas-Barbosa, J. Janek and W. G. Zeier, *Chem. Mater.*, 2019, **31**, 8328–8337.
28. L. Zhou, T.-T. Zuo, C. Y. Kwok, S. Y. Kim, A. Assoud, Q. Zhang, J. Janek and L. F. Nazar, *Nat Energy*, 2022, **7**, 83–93.
29. Y. Tanaka, K. Ueno, K. Mizuno, K. Takeuchi, T. Asano and A. Sakai, *Angew Chem Int Ed*, 2023, **62**, e202217581.
30. K.-H. Park, K. Kaup, A. Assoud, Q. Zhang, X. Wu and L. F. Nazar, *ACS Energy Lett.*, 2020, **5**, 533–539.
31. I. Kochetkov, T.-T. Zuo, R. Ruess, B. Singh, L. Zhou, K. Kaup, J. Janek and L. Nazar, *Energy Environ. Sci.*, 2022, **15**, 3933–3944.
32. B. Hennequart, M. Platonova, R. Chometon, T. Marchandier, A. Benedetto, E. Quemina, R. Dugas, C. Lethien and J.-M. Tarascon, *ACS Energy Lett.*, 2024, **9**, 454–460.
33. J. Hüttel, C. Seidl, H. Auer, K. Nikolowski, A. L. Görne, M. Arnold, C. Heubner, M. Wolter and A. Michaelis, *Energy Storage Materials*, 2021, **40**, 259–267.
34. M. Palmer, L. Qian, V. K. Singh, L. Merola, E. Carlson, C. Haslam, J. Janek, L. F. Nazar and J. Sakamoto, *Solid State Ionics*, 2025, **428**, 116948.
35. L. Merola, V. K. Singh, M. Palmer, J. K. Eckhardt, S. L. Benz, T. Fuchs, L. F. Nazar, J. Sakamoto, F. H. Richter and J. Janek, *ACS Appl. Mater. Interfaces*, 2024, acsami.4c11597.
36. T. Lee, S. Joo, S. Kang, T. Kim, Y. Park, Y. Chae, K. Kim, W. Cho and S. Kim, *ACS Appl. Energy Mater.*, 2025, **8**, 5585–5611.
37. J. K. Eckhardt, S. Kremer, L. Merola and J. Janek, *ACS Appl. Mater. Interfaces*, 2024, **16**, 18222–18235.
38. J. Fleig and J. Maier, *J. Electrochem. Soc.*, 1997, **144**, L302–L305.
39. M. Klimpel, C. Černe, J. Šivavec, J. F. Baumgärtner, H. Zhang, R. Widmer, F. Okur, F. Krumeich, K. V. Kravchyk and M. V. Kovalenko, *ACS Appl. Energy Mater.*, 2025, acaem.5c02435.
40. D. P. Abraham, D. W. Dees, J. Knuth, E. Reynolds, R. Gerald, Y.-E. Hyung, I. Belharouak, M. Stoll, E. Sammann, S. MacLaren, R. Haasch, R. Twisten, M. Sardela, V. Battaglia, E. Cairns, J. Kerr, M. Kerlau, R. Kostecki, J. Lei, K. McCarthy, F. McLarnon, J. Reimer, T. Richardson, P. Ross, S. Sloop, X. Song, V. Zhuang, M. Balasubramanian, J. McBreen, K.-Y. Chung, X. Q. Yang, W.-S. Yoon and L. Norin, *Diagnostic examination of Generation 2 lithium-ion cells and assessment of performance degradation mechanisms.*, 2005.
41. Y. Leng, S. Ge, D. Marple, X.-G. Yang, C. Bauer, P. Lamp and C.-Y. Wang, *J. Electrochem. Soc.*, 2017, **164**, A1037–A1049.
42. J. B. Quinn, T. Waldmann, K. Richter, M. Kasper and M. Wohlfahrt-Mehrens, *J. Electrochem. Soc.*, 2018, **165**, A3284–A3291.
43. I. You, B. Singh, M. Cui, G. Goward, L. Qian, Z. Arthur, G. King and L. F. Nazar, *Energy Environ. Sci.*, 2025, **18**, 478–491.
44. B. Singh, Y. Wang, J. Liu, J. D. Bazak, A. Shyamsunder and L. F. Nazar, *J. Am. Chem. Soc.*, 2024, **146**, 17158–17169.
45. T. Dai, S. Wu, Y. Lu, Y. Yang, Y. Liu, C. Chang, X. Rong, R. Xiao, J. Zhao, Y. Liu, W. Wang, L. Chen and Y.-S. Hu, *Nat Energy*, 2023, **8**, 1221–1228.
46. W. Kim, S. Han, S. Lee, J. Yoo, C. Park, S. Yu, D. Won, E. Lee, K. Ko, J. Noh, G. Choi, M. Kim and K. Kang, *Energy Environ. Sci.*, 2025, **18**, 8039–8051.
47. J.-M. Doux, Y. Yang, D. H. S. Tan, H. Nguyen, E. A. Wu, X. Wang, A. Banerjee and Y. S. Meng, *J. Mater. Chem. A*, 2020, **8**, 5049–5055.
48. Y. Wang, H. Hao, K. G. Naik, B. S. Vishnugopi, C. D. Fincher, Q. Yan, V. Raj, H. Celio, G. Yang, H. Fang, Y. Chiang, F. A. Perras, P. Jena, J. Watt, P. P. Mukherjee and D. Mitlin, *Advanced Energy Materials*, 2024, **14**, 2304530.



49. C. Rosenbach, F. Walther, J. Ruhl, M. Hartmann, T. A. Hendriks, S. Ohno, J. Janek and W. G. Zeier, *Advanced Energy Materials*, 2023, **13**, 2203673.
50. S. Pacetti, C. Karlsson, E. Mijit, M. Drüschler, A. Di Cicco, N. Pinto, D. Bresser and J. Rezvani, *J. Phys. Chem. C*, 2026, **130**, 3040–3049.
51. I. Rashid, R. R. Haddadin, A. A. Alkafaween, R. N. Alkaraki and R. M. Alkasasbeh, *AAPS Open*, 2022, **8**, 6.
52. M. Papakyriakou, M. Lu, Y. Liu, Z. Liu, H. Chen, M. T. McDowell and S. Xia, *Journal of Power Sources*, 2021, **516**, 230672.
53. S.-Y. Lee, J.-H. Han, H.-W. Gong, J. Ahn, K.-W. Yi and Y. W. Cho, *J. Mater. Chem. A*, 2025, **13**, 6342–6346.
54. K. Hikima, M. Totani, S. Obokata, H. Muto and A. Matsuda, *ACS Appl. Energy Mater.*, 2022, **5**, 2349–2355.
55. P. Barai, T. Kinnibrugh, M. Wolfman, J. Garcia, X. Wang, T. T. Fister, H. Iddir and V. Srinivasan, *JOM*, 2024, **76**, 1180–1191.
56. T. Zuo, F. Walther, J. H. Teo, R. Rueß, Y. Wang, M. Rohnke, D. Schröder, L. F. Nazar and J. Janek, *Angew Chem Int Ed*, 2023, **62**, e202213228.
57. Y. U. Wang, *Acta Materialia*, 2006, **54**, 953–961.
58. F. Raether, G. Seifert and H. Ziebold, *Advcd Theory and Sims*, 2019, **2**, 1900048.
59. A. Gupta and J. Sakamoto, *The Electrochemical Society Interface*, 2019, **28**, 63.
60. T. Krauskopf, H. Hartmann, W. G. Zeier and J. Janek, *ACS Appl. Mater. Interfaces*, 2019, **11**, 14463–14477.
61. L. Pastewka and M. O. Robbins, *Proc. Natl. Acad. Sci. U.S.A.*, 2014, **111**, 3298–3303.
62. B. N. J. Persson, *Surface Science Reports*, 2006, **61**, 201–227.
63. H. Huo, J. Luo, V. Thangadurai, X. Guo, C.-W. Nan and X. Sun, *ACS Energy Lett.*, 2020, **5**, 252–262.
64. S. Wang, E. Barks, P.-T. Lin, X. Xu, C. Melamed, G. McConohy, S. Nemsák and W. C. Chueh, *Chem. Mater.*, 2024, **36**, 6849–6864.
65. S. Jeon, K.-H. Park, W. Cho, G. Jeong, J. Yu, Y. J. Park and K. Kim, *Solid State Ionics*, 2025, **421**, 116791.
66. J. A. Newnham, J. Kondek, J. Hartel, C. Rosenbach, C. Li, V. Faka, L. Gronych, D. Glikman, F. Schreiner, D. D. Wind, B. Braunschweig, M. R. Hansen and W. G. Zeier, *Chem. Mater.*, 2025, **37**, 4130–4144.
67. S. Adams, *Energy Storage Materials*, 2024, **68**, 103359.
68. M. Siniscalchi, J. S. Gibson, J. Tufnail, J. E. N. Swallow, J. Lewis, G. Matthews, B. Karagoz, M. A. Van Spronsen, G. Held, R. S. Weatherup, C. R. M. Grovenor and S. C. Speller, *ACS Appl. Mater. Interfaces*, 2024, **16**, 27230–27241.
69. A. Shyamsunder, M. Palmer, I. R. Kochetkov, J. S. Sakamoto and L. F. Nazar, *ACS Appl. Mater. Interfaces*, 2023, acsami.3c12278.
70. H. Huo, Y. Chen, N. Zhao, X. Lin, J. Luo, X. Yang, Y. Liu, X. Guo and X. Sun, *Nano Energy*, 2019, **61**, 119–125.
71. Y. Ruan, Y. Lu, X. Huang, J. Su, C. Sun, J. Jin and Z. Wen, *J. Mater. Chem. A*, 2019, **7**, 14565–14574.
72. S. Koch, *Solid State Ionics*, 2004, **168**, 1–11.
73. P. Minnmann, J. Schubert, S. Kremer, R. Rekers, S. Burkhardt, R. Ruess, A. Bielefeld, F. H. Richter and J. Janek, *J. Electrochem. Soc.*, 2024, **171**, 060514.
74. H. Kim, S. Park, S. Kang, J. Y. Jung, K. Kim, J. Yu, D. Kim, J. Lee, Y. Sun and W. Cho, *Adv Funct Materials*, DOI:10.1002/adfm.202409318.
75. F. Walther, S. Randau, Y. Schneider, J. Sann, M. Rohnke, F. H. Richter, W. G. Zeier and J. Janek, *Chem. Mater.*, 2020, **32**, 6123–6136.
76. M. Kissel, M. Schosland, J. Töws, D. Kalita, Y. Schneider, J. Kessler-Kühn, S. Schröder, J. Schubert, F. Frankenberg, A. Kwade, A. Bielefeld, F. H. Richter and J. Janek, *Advanced Energy Materials*, 2025, **15**, 2405405.

View Article Online  
DOI: 10.1039/D5EE07777J

77. H.-C. Yu, S. B. Adler, S. A. Barnett and K. Thornton, *Electrochimica Acta*, 2020, **354**, 136534.
78. C. Haslam and J. Sakamoto, *J. Electrochem. Soc.*, 2023, **170**, 040524.
79. D.-S. Ko, S. Kim, S. Lee, G. Yoon, D. Kim, C. Shin, D. Kim, J. Lee, S. Sul, D.-J. Yun and C. Jung, *Nat Commun*, 2025, **16**, 1066. View Article Online  
DOI: 10.1039/D5EE07777J
80. S. E. Sandoval, J. A. Lewis, B. S. Vishnugopi, D. L. Nelson, M. M. Schneider, F. J. Q. Cortes, C. M. Matthews, J. Watt, M. Tian, P. Shevchenko, P. P. Mukherjee and M. T. McDowell, *Joule*, 2023, **7**, 2054–2073.
81. S. H. Choi, C. H. Baek, J. Oh, G.-J. Lee, M. Kim, H. Lee, D.-J. Yoo, Y. S. Jung, K. Kim, J.-S. Yu, W. Cho, H. Park and J. W. Choi, *Nat Commun*, 2025, **16**, 5871.
82. J. Thomas, S. S. Behara and A. Van Der Ven, *Chem. Mater.*, 2024, acs.chemmater.4c01903.
83. A. D. Pelton, *Bulletin of Alloy Phase Diagrams*, 1986, **7**, 223–228.
84. S. Jin, Y. Ye, Y. Niu, Y. Xu, H. Jin, J. Wang, Z. Sun, A. Cao, X. Wu, Y. Luo, H. Ji and L.-J. Wan, *J. Am. Chem. Soc.*, 2020, **142**, 8818–8826.
85. K. Yan, Z. Lu, H.-W. Lee, F. Xiong, P.-C. Hsu, Y. Li, J. Zhao, S. Chu and Y. Cui, *Nat Energy*, 2016, **1**, 16010.
86. Y.-G. Lee, S. Fujiki, C. Jung, N. Suzuki, N. Yashiro, R. Omoda, D.-S. Ko, T. Shiratsuchi, T. Sugimoto, S. Ryu, J. H. Ku, T. Watanabe, Y. Park, Y. Aihara, D. Im and I. T. Han, *Nat Energy*, 2020, **5**, 299–308.
87. M. S. R. Limon, C. W. Duffee and Z. Ahmad, *ACS Energy Lett.*, 2025, **10**, 1999–2006.
88. W. Kim, J. Noh, S. Lee, K. Yoon, S. Han, S. Yu, K. Ko and K. Kang, *Advanced Materials*, 2023, **35**, 2301631.
89. Z. Song, T. Wang, H. Yang, W. H. Kan, Y. Chen, Q. Yu, L. Wang, Y. Zhang, Y. Dai, H. Chen, W. Yin, T. Honda, M. Avdeev, H. Xu, J. Ma, Y. Huang and W. Luo, *Nat Commun*, 2024, **15**, 1481.
90. L. Zhou, J. D. Bazak, C. Li and L. F. Nazar, *ACS Energy Lett.*, 2024, **9**, 4093–4101.
91. T. Shi, Y.-Q. Zhang, Q. Tu, Y. Wang, M. C. Scott and G. Ceder, *J. Mater. Chem. A*, 2020, **8**, 17399–17404.
92. C. König, V. Miß, L. Janin and B. Roling, *ACS Appl. Energy Mater.*, 2023, **6**, 9356–9362.
93. A. Ch. Lazanas and M. I. Prodromidis, *ACS Meas. Sci. Au*, 2023, **3**, 162–193.



**Data Availability Statement:**

The data supporting this article have been included as part of the Supplementary Information.

